Towards Seismic Detection with Fibre Sensing

Miguel García Alonso

UROPS at CQT / NUS - **July 2023**

Supervisor:

Professor Christian Kurtsiefer

Abstract

With a fibre-based heterodyne phasemeter, measurements of the optical path difference between a sensing arm and a reference arm can be done to register displacements in the sensing fibre. This data is collected in the form of a phase difference. Moreover, the phase is directly related to the length variations in the sensing fibre.

Sub-wavelength length changes in deployed fibres can be measured by this method, enabling their use as seismic detectors. Compared to traditional seismographs, the use of already existing optical fibres could prove very inexpensive, especially for underwater detection systems. For this purpose, understanding how earthquakes are measured and separated from background noise is fundamental.

This report explains the code written to automatically register earthquakes by combining the data from seismographs installed around Singapore. It also describes the techniques needed for the distinction between these events and noise.

Furthermore, it expands on the initial noises observed on the phase reconstruction data from the fibre sensing and the steps followed to solve them.

Finally, it documents some of the events that can be detected with the fibre.

Contents

1. Introduction ... 3

1.1. Fibre sensing purpose ... 3

1.2. Michelson interferometer ... 3

1.3. Content outline ... 5

2. Identifying events from seismographs data ... 6

2.1. Code development ... 6

2.1.1. Data extraction ... 6
2.1.2. Data processing ... 7
2.1.3. Individual confirmation and final plots ... 10

2.2. Results ... 12

2.2.1. Case 1. Strong event during nighttime. ... 12
2.2.2. Case 2. Strong event during daytime. ... 17
2.2.3. Case 3. Further strong event during daytime. ... 19
2.2.4. Case 4. Weaker and closer events. ... 21

2.3. Conclusion on effectiveness of the code ... 25

3. Fibre sensing setup ... 26

3.1. Heterodyne phasemeter ... 26

3.2. Demodulation ... 27

3.3. Noise in the phase reconstruction ... 28

3.3.1. Early noise measurements ... 28
3.3.2. Early conclusions ... 30
3.3.3. Solution attempts and observations ... 30

4. Detections with fibre sensing ... 32

4.1. Noise in the phase and velocity ... 32

4.2. Detections ... 36

4.3. 20 km sensing arm measurements ... 39

5. Summary and next steps ... 43

6. Appendix ... 44

6.1. Notes on parameter selection and errors ... 44

7. Bibliography ... 45

1. Introduction

1.1. Fibre sensing purpose

Fibre sensing is presented as way to detect acoustic noises or environmental disturbances in the vicinities of a fibre. Of special interest is the use of the already deployed optical commercial fibres. In the recent years, this idea has advanced in different fields in science, one of them being geophysics.

Seismometers are very common and easy to maintain in land, this is not the case underwater. Due to the costs of installing submarine detection systems, providing information for geologist's research on large areas under the oceans is not economically viable. The use of the 'SMART' [1] (Scientific Monitoring and Reliable Telecommunications) cables has been proposed to tackle this problem. By including environmental sensors every few tens of kilometres, these cables provide reliable optical fibres for seismic and acoustic detection. Since 2016, multiple advances have been made on this sense. Some groups have been able to use multiple 1000 km fibres to detect earthquakes by analysing the instability of metrology-grade lasers [2]. Others have been able to use short 20 km optical fibres to map fault areas [3].

Even if detecting earthquakes is a possibility, fibre sensing could potentially also be used for acoustic noise identification or human traffic patterns recognition. This group at CQT is currently developing a fibre sensing project that tries to expand in the use of optical fibres for events detection via laser interferometry [4].

1.2. Michelson interferometer

The fibre sensing project consists of a heterodyne phasemeter [5, 6]. A heterodyne phasemeter is obtained by a modification of a Michelson interferometer.

A Michelson interferometer measures the optical path difference between two arms.

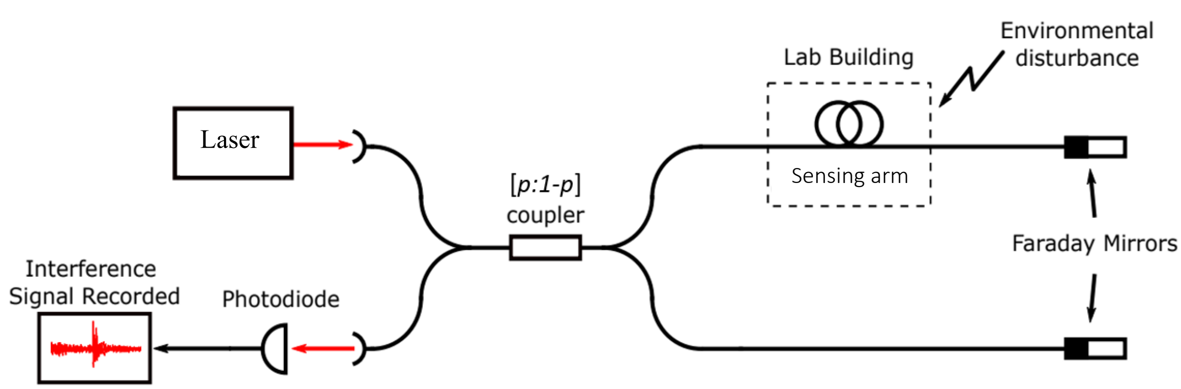

Figure 1. Diagram of a Michelson interferometer.

The experiment begins with a laser that emits light with a known power and known wavelength. We will call this power P_{in}, and its corresponding electrical field E_{in}. Equivalently, we will call P_{out} and E_{out} the power and electric fields after the interference. An optical isolator is also included after the laser to avoid back reflection into it.

First, the laser light passes through an optical coupler, or $[p: (1-p)]$ coupler. This light is now divided into the two arms. The *p* parameter varies depending on the length of the sensing arm. The longer the arm, the higher the power that needs to be provided to account for the loss during the route and so *p* is modified accordingly. We will call the shorter arm L_1 and the longer one L_2. The difference between the two will be called:

$$\Delta L = L_2 - L_1 \tag{1}$$

At the end of each arm, a Faraday Mirror is installed. This is to solve the birefringence [7], originated by the travel of the light through the fibre, which can cause the light to be polarized to an undesirable angle. This polarization difference would generate problems later when analysing the interference of both arms. The Faraday mirrors (Fig.1) add a π/2 rotation to the polarization of the light on each end of the arms before returning the light back. As a result, by the end of the travel, any extra polarization will be cancelled and the state of the light leaving both arms is just orthogonal to the one that had entered.

Now, the light from the two paths interferes at the coupler again and goes into a photodiode, where the output optical power can be analysed. The fluctuations of this power can be obtained with the corresponding electrical fields. These fields are obtained noticing that the wavenumber of the light is given by:

$$k = nk_0 = n\frac{2\pi}{\lambda_0} \tag{2}$$

Where *n* for the optical fibre has a value of $n = 1.52$ and λ_0 is the wavelength from the laser on the vacuum. The angular velocity of the light will be $\omega = \omega_1 = \omega_2 = kc$ (1 refers to short arm, while 2 the long one). The electric field formulas now are then the classical ones, where we must notice that the path travelled for each arm is $2L_1$ and $2L_2$ respectively. Moreover, given that the parameter from the coupler *p* is adjusted to receive at the photodiode the same power from each arm, then:

$$E_{out}(t) = \frac{E_{in}}{2}e^{i(\omega t - k2L_1)} + \frac{E_{in}}{2}e^{i(\omega t - k2L_2)} \tag{3}$$

Simplifying, we get:

$$E_{out}(t) = \frac{E_{in}}{2} e^{i(\omega t - k2L_1)}\left(1 + e^{-ik2\Delta L}\right)$$

(4)

Now, by defining the phase difference as $\theta = k2\Delta L$, and noticing that the power output is the complex square of the electric field, after simplifying:

$$P_{out} = \frac{P_{in}}{2}(1 + cos(\theta))$$

(5)

By measuring the output power, we would be able to obtain the path difference and therefore any length change in the fibres. From this changes, we can infer what could have caused the displacement.

However, at the points where the output power is on its maximum and equals the input, or at its minimum, and equals 0, the variation in length becomes ambiguous. This is because any small change on P_{out} from this maximum could be caused by a small increase in θ, or equivalently, by a small decrease in θ, both resulting in a decrease in power due to the properties of the cosine function. The same reasoning can be applied for when the power is at its minimum.

To be able to measure the phase without this problem we will need to use a heterodyne phasemeter, but the main ideas behind the measurement agree with those of the Michelson interferometer.

1.3. Content outline

The document will start in section 2 explaining an earthquake detection code that uses the data from seismographs. It will also present the techniques needed to identify the arrival of an earthquake wave to a seismograph and document how this will be used later in the fibre sensing experiment. It will also provide some examples of detections on the seismographs.

Section 3 will present the heterodyne phasemeter. It will also expand on the initial measurements done with the phase reconstruction. Moreover, it will describe the noises that were identified and the solutions that were implemented.

Finally, section 4 will document some of the events that were detected using different fibres and it will explain the use of a velocity approximation for easier event identification.

2. Identifying events from seismographs data

Initially, the goal was to write a code that could potentially register earthquakes and help the user figure out the distance from the detectors to the epicentre of these events. This code would have its use when trying to find events with the fibre sensing project. With the code, the exact arrival of a wave to the lab could be recorded. This time record would later let the user confirm if a measurement on the fibre sensing data corresponded to an earthquake or not (by direct comparison with the seismograph data).

In this section, many of the different techniques used to detect earthquakes will also be explored, which will prove very useful when analysing the phase reconstruction data on section 4. With these techniques and code, many events not reported by the Singapore Meteorological Service will be detected with the seismographs, letting us have a larger set of earthquakes that we can later use to test the fibre sensing detections capabilities. The next sections explain how the code works. Moreover, they expand on how events should be analysed to clearly distinguish between noise and earthquakes.

2.1. Code development

2.1.1. Data extraction

To run the program, the user changes the initial time and duration desired as well as two analysis parameters (more on these parameters on Appendix 1). The program will start by extracting the data from the seismographs. For it, it will make use of Obspy [8], a python framework commonly used between geologists. The data will be directly downloaded from the IRIS (Incorporated Research Institutions for Seismology) servers, and it will contain the information of four detectors (fig.3): R9F0D only on the channel EHZ (vertical geophone); and R9273 (at NUS), BESC and KAPK, each on the three on the channels EHZ, EHN (latitudinal geophone) and EHE (longitudinal geophone).

The first two detectors are from the Raspberry Shake network, a private company's network of semi-professional seismometers whose data can be publicly accessed. Of special interest is R9273, as this seismometer was installed by our group next to the lab, and so the arrival of waves to this detector should correspond in time to those arriving to the fibre sensing experiment. The last two detectors, KAPK and BESC, are from the MS (Meteorological Service Singapore) network.

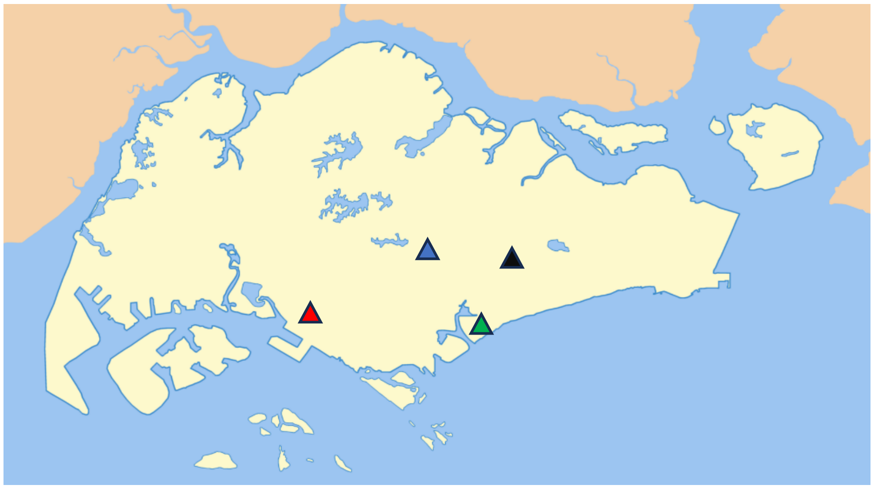

Figure 2. Location of the detectors used for the code. R9273 and CQT lab (red), KAPK (green), BESC (blue) and R9F0D (black).

2.1.2. Data processing

To begin with, a bandpass filter between 0.5 and 12 Hz is applied directly on the data as earthquakes waves tend to distribute between 0.5 and 8Hz [9] (the extra 4Hz do not impact the measurement and are useful for context on background noise levels). This initial data extracted from the seismographs is in the form of counts per time. Counts correspond to the voltage values registered on the seismograph and can be directly related to velocity. The way the program will analyse the data now follows the next steps.

First, the code will start with the R9273 (NUS) detector. It will begin with the 'classic sta-lta' function. This function takes the data from the seismometer and finds the ratio between the sta and the lta. Sta is a short-term analyser of the wave amplitude, while lta is a longer period noise analyser [10]. This function gives a number for the ratio on each time interval, and if this number goes above or under some pre-determined trigger limits, the program will identify the point as a 'trigger on' or 'trigger off' point respectively (fig.4). 'Classic sta-lta' will prove to be the more consistent of the functions presented on this section. It is not especially good at detecting faint events, or events in a high-background noise, but it will be clearly able to separate an earthquake from noise if it is strong enough.

A coincidence trigger function implemented through Obspy is applying simultaneously the previous function to the three channels of the detector. If the function detects that there is a coincidence in between triggers in the three channels, it will save the event as a possible result. After the process, it will give us a set of data (denoted 'Initial list 1' on fig.3) that includes a list of possible events with the starting and ending time of each, based on if the triggers have been activated on all three channels or not.

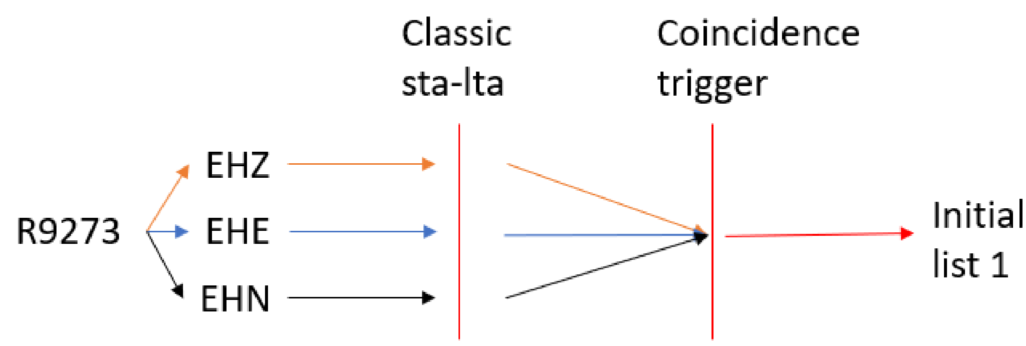

Figure 3. Diagram representing initial detection steps.

Figure 4 is a visual example of how the trigger works on each channel. The upper part represents the data from the Sumatra earthquake (2.2.1) on the detector R9273 on channel EHZ. On the lower part of the figure, the function takes the data from the upper part and plots the sta-lta ratio. If this ratio goes over the stablished trigger (red line), an event will start to be recorded until it goes back under the blue line.

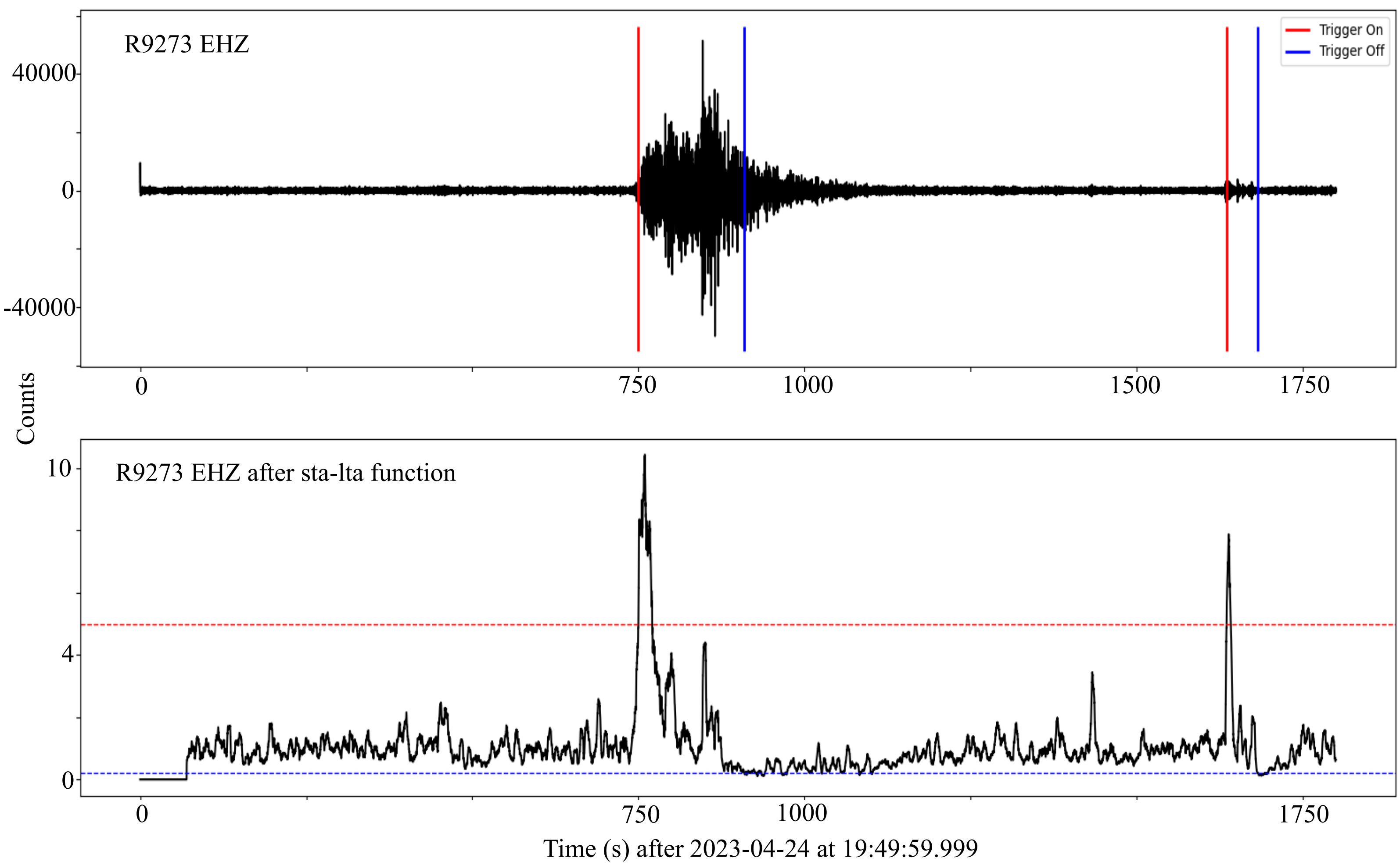

Figure 4. Triggering example with classic sta-lta method on an extract of the Sumatra Earthquake. This earthquake will be analysed in detail in the next chapter.

The counts plot can be seen in the upper part of fig.4. Some noise is also registered as a possible earthquake after the 1500 seconds mark, but this will be discarded with the later comparison. The coincidence trigger function runs the method on the three channels and compares it before saving it as an event, which usually discards this type of noise (fig.3). After the coincidence trigger and before saving the 'Initial list 1', the code will condense the data so that if two trigger events overlap in time they are just classified as one. This step also accounts for uncertainties in the detection of multiple peaks of the same event. This will give us our first set of checked events (Initial list 1). But further cleaning must still be done to avoid misidentifying some of the possible saved noises as earthquakes.

The program will now use the 'z-detect' function [10]. The whole idea on what the program does with the trigger coincidence function now is the same, but this time it uses the z-detect function. The z detect function will increment any small variation in amplitude of the counts with respect to the surrounding values. This will prove to be very effective when an event is much greater than the background noise. This also means that many of the smaller spikes caused by traffic are registered as possible events. However, this can be good when trying to find fainter events, and so there is a parameter in the code would let us just use this function and ignore the others. After the coincidence triggers are done, this time on this different function but still on the same detector, this will give the second set of possible events (Initial list 2).

A last check is done by following the 'carl-sta' function [10]. Using the same procedure as before, this will give the third set of possible events for this detector (Initial list 3). This is usually the least effective function in noisy conditions, but it is still good for checking in silent environments, and so a parameter on the code can let us deactivate it if needed. After the three methods have run, the program now has three sets of possible events for detector R9273. The code will also provide us with this information by printing the starting time of these events and their durations.

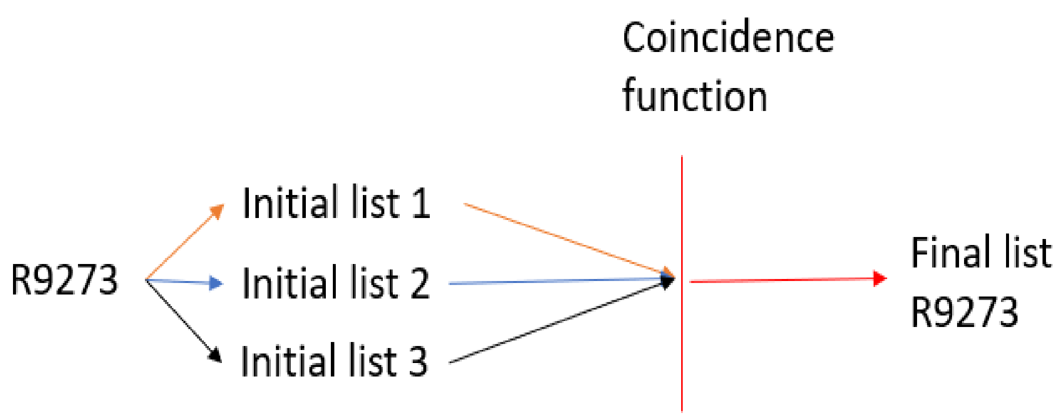

Figure 5. Diagram representing the combination of the three lists, each coming from a different function applied on the three channels.

The program will now check which of these events agree between the three lists and save those in a R9273 list of events (Final list R9273). This will constitute our set of possible events for detector R9273 on its three channels (fig.6).

After this, the code will repeat the process of the three functions with the detectors BESC and KAPK independently. The code is identical, but the parameters of the functions are changed, as the noise levels and sensitivity of each of the detectors varies significantly.

At this point the program has three sets of possible events, one for each detector. Taking the BESC detector as the better one, given its noise levels usually being smaller, we will compare its events with those of the other two sets (fig.7). The code will save the confirmed events as the final set. In this step, we also must account for events not being measured at the same time on every detector. This is because of the time difference in the arrival of the same wave to each detector (as the detectors are not all in the same place) and the difference in the triggering sensitivity of the code for each one.

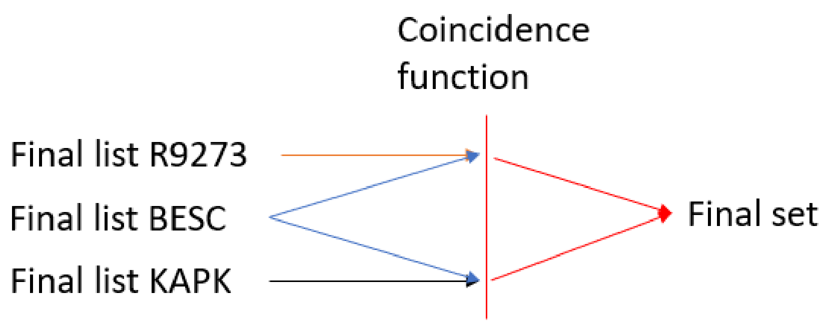

Figure 6. Combination of the lists coming from each detector.

2.1.3. Individual confirmation and final plots

This final set already contains events that have been detected by at least two seismographs on their three channels (BESC and R9273 or BESC and KAPK). But, just in case there was a simultaneous spike of noise that our methods could not filter, a last check will be made. For it, the data on R9F0D will be used (fig.3).

As this detector only has the EHZ channel operational, we will individually apply each of the three functions (classic sta-lta, z-detect, and carl-sta) to it. The data provided to the functions will be just a few hundred seconds before and after the events on the previous list, to avoid any unnecessary calculations. After comparing the events of the functions with the original final list, we remove those events that cannot be confirmed. This will give us a definitive final list of events confirmed by at least three detectors (fig.7).

Note that, in case this last step does not confirm any event because all the previous final events were noise, or just because the R9F0D accumulates too much background noise, the code will still provide us with an approximate time and duration of the unconfirmed final list of events (Final set).

But, if the events are confirmed, the code will attempt to guess when the p and s waves might have first arrived and the possible distance from each detector to the epicentre. To do this, it will take the unfiltered data from each channel of a detector and introduce it into the Obspy imported 'p-s picker function' [11]. The data taken was unfiltered as the function already filters it based on some parameters that we can modify accordingly. This function is designed for professional seismographs where the background noise is greatly reduced even before the data is collected. As a result, it is not very precise in the case of the three main detectors we are using but it is still of help to the user.

The results are then printed as well as a spectrogram and plot that includes the guessed p and s wave arrival for each channel of each detector. The distance from the epicentre to the detectors is calculated by taking the time difference between the p and s waves first arrivals and then multiplying by 8.4, as this is a good enough approximation for Earth's crust [12]. This number comes from the speed of the s waves being slower than the p waves by a known factor. It should be noted that the global spectrogram (a spectrogram of the whole period that is being analysed) of R9273 EHZ is always plotted to help identify possible missed candidates.

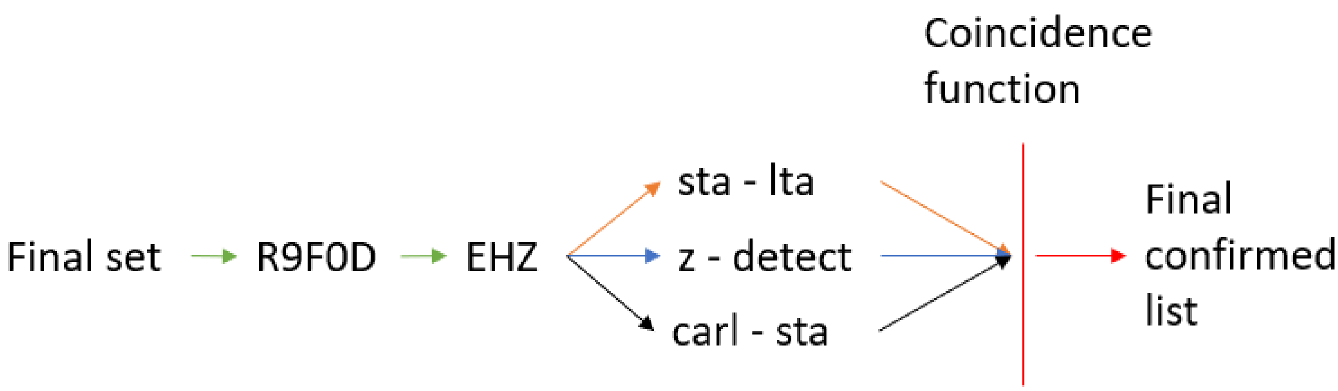

Figure 7. Diagram of the last confirmation step using R9F0D.

The interpretation of these results and the accuracy of the method will be analysed next.

2.2. Results

The previous code needs of some parameters to be adjusted for the triggering functions to work. The main event used for this parameter selection is Case 1 in the following section. After these parameters were set, I the program was tested over the months of April, May, and early June 2023. The code was tested on diverse situations, including daytime events with high background noise and closer faint events. Some of these examples are shown next.

2.2.1. Case 1. Strong event during nighttime.

The best example of the use of the program is the night of the 24th of April. A 7.3 magnitude earthquake (IRIS ID 11687680)[1] occurred at an approximate distance of 631 km from the Singapore bay and 34km in depth in Sumatra. In this section I will refer to this earthquake as the 'Sumatra Event'.

This event was used to set most of the parameters for the triggering functions. In most cases, a function applied to the channels of a detector will detect up to a hundred coincidences in the triggers. An example of this in this event is the KAPK detector. When analysing the whole night, the classic sta-lta method detects eighty-nine events (as it is very sensitive to change in low background noise conditions), but the other methods give more accurate assessments (one event for z-detect and two events for carl-sta). The coincidence functions applied to these lists will account for these discrepancies.

After the code applies all the filtering (explained in the previous section), it will finally print its results and plot the suggested event. In this case, the three detectors agree that the only event during the night is the Sumatra earthquake, and this is confirmed by R9F0D. However, none of them pick the correct p and s waves. This was expected as the p-s picker function cannot properly work under these noisy conditions.

Counts plots and spectrogram for each channel is given by the code on the suggested event. Note that the start time of the earthquakes saved by the code is also not exact (this is intended as it better helps when comparing events between detectors), and the plots are given with a couple of seconds of margin to account for it. Looking at the spectrogram and plot of BESC channel EHZ the results can be better explained.

In the spectrogram on fig.8 (data not filtered in it), we will notice that there is only colour difference in the low frequencies. The spectrograms plotted in this document use colour to indicate relative intensity to the other frequencies seen in the graph. Consequently, the lack of lighter colours on the upper frequencies means that the lower ones dominate. This is because the earthquake energy on arrival was much stronger than the background noise (which is why I chose this event as an example). Remark that the red and purple

[1] For the complete list of events refer to http://ds.iris.edu/seismon/eventlist/index.phtml , this page will just save the last month so other pages to access previous versions of this webpage should be used.

line show the attempts of the code to indicate the arrival of the p and s waves and should only be used as a guide.

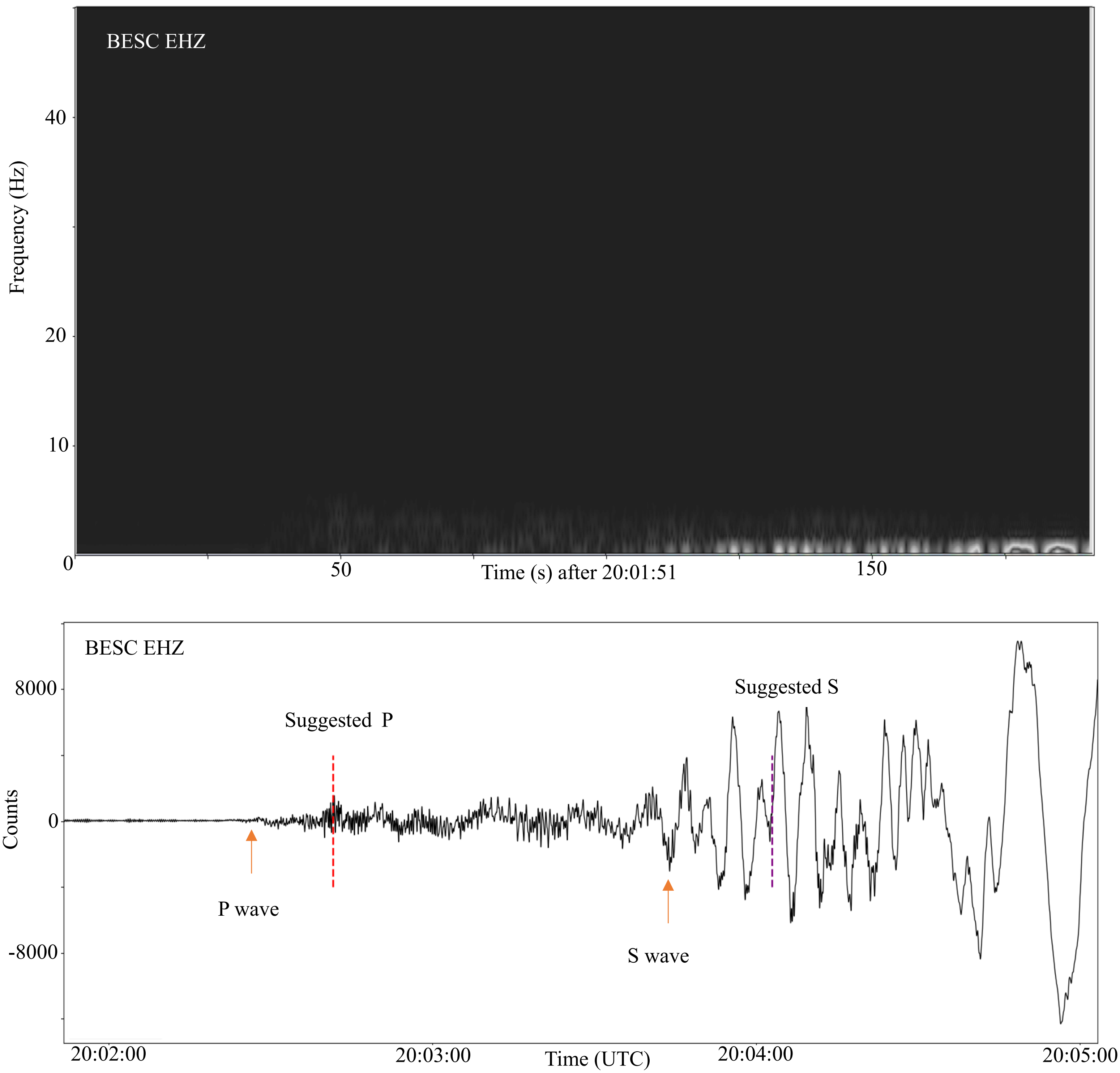

Figure 8. Spectrogram and counts plot of the Sumatra Event on BESC detector channel EHZ. Whiter colours imply higher intensity of waves in those frequencies.

From these plots now, we can zoom and use the guiding to better determine the p and s waves arrival. The spectrogram is usually a good tool to identify when the p waves appear, as their arrival is noticed by a slight increase in the frequencies between 0.5 and 3 Hz.

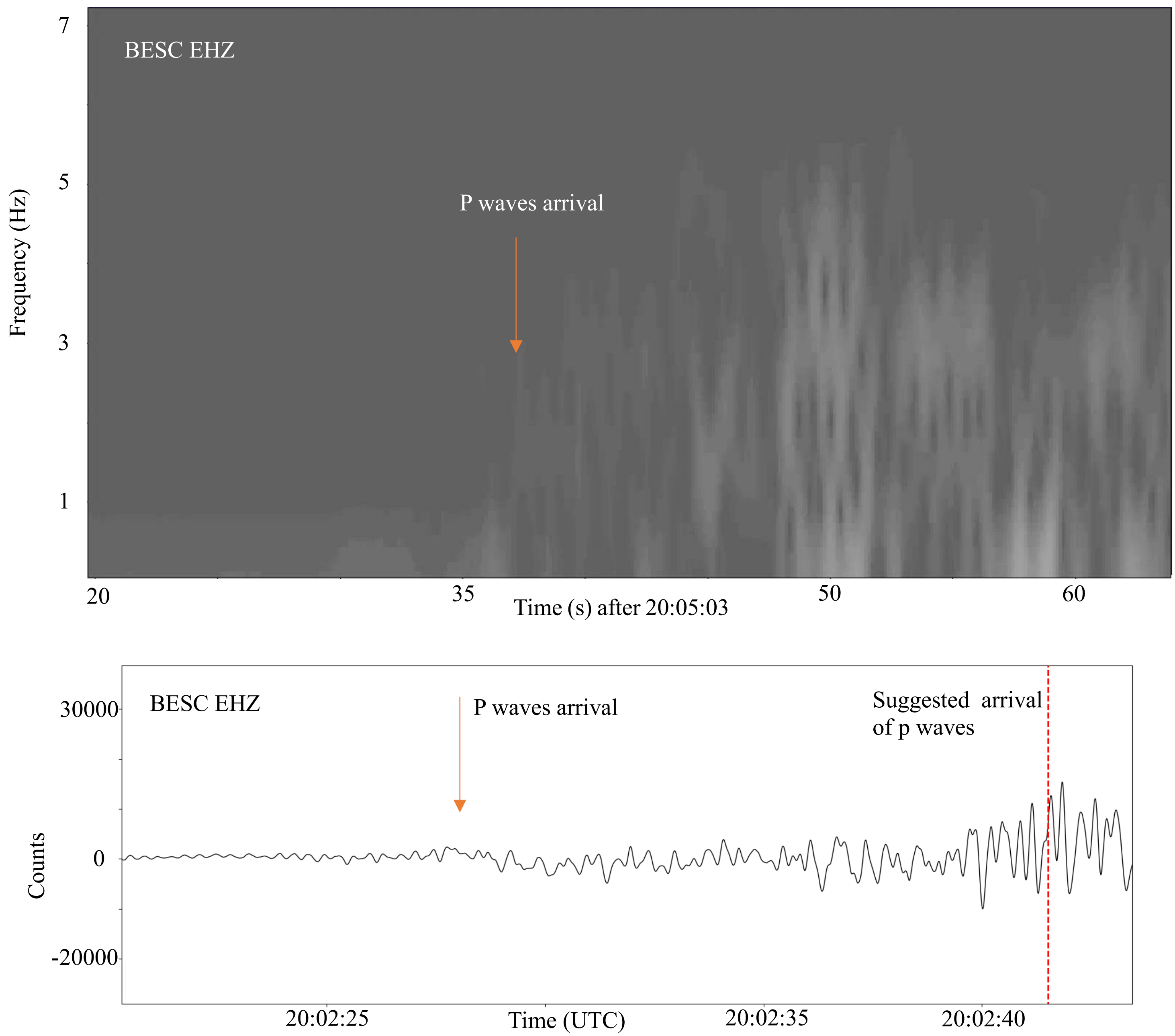

Figure 9. Zoom in on spectrogram and counts plot for BESC EHZ detector on Sumatra Event for the p waves arrival (orange arrow). On the spectrogram.

Note that the spectrograms do not have the filters applied to be able to properly detect the p wave. The p wave is seen to arrive at time 20:02:27. The p wave is much harder to identify just looking at the counts plot, as noise usually makes it difficult to distinguish it. Now, with the counts plot, the s waves will be seen by a sudden increase in amplitude. The s waves cannot be recognized in the spectrogram as their frequency agrees with that of the p and other surface waves.

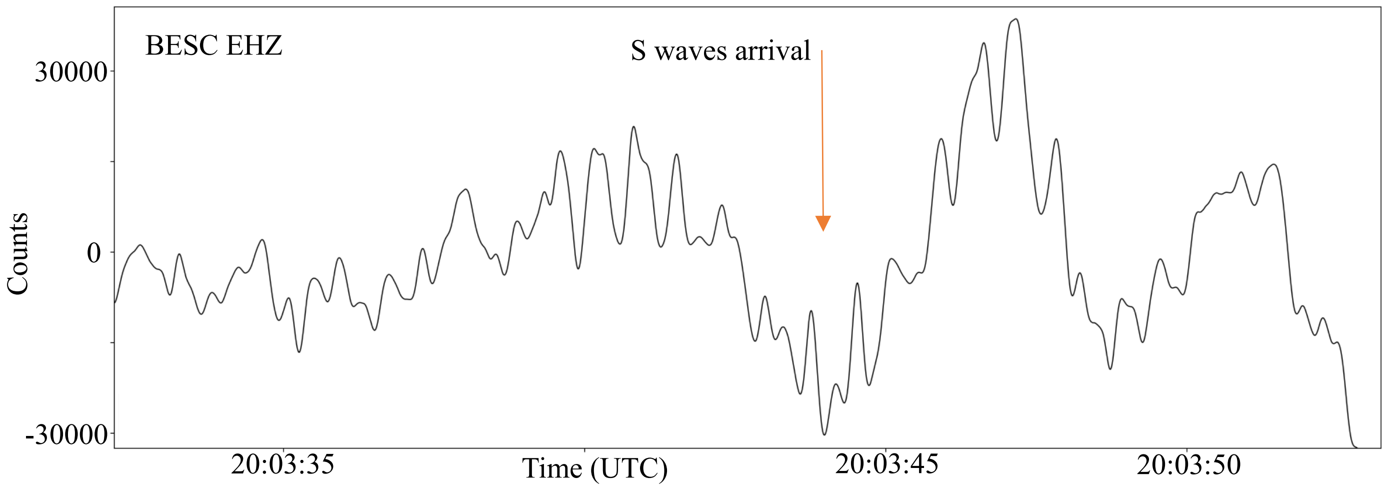

Figure 10. Zoom on the counts plot for BESC EHZ on Sumatra event for the s waves arrival.

The s wave can be seen arriving at 20:03:44. Now, the total time difference is 77 seconds. Multiplying by 8.4 we get 646.8 km from the BESC detector to the epicentre. The actual distance is approximately 641km to Beatty Secondary School (BESC), so the measurement is off by less than 10 km. The same process can now be done for the other detectors and find the distance in a similar way.

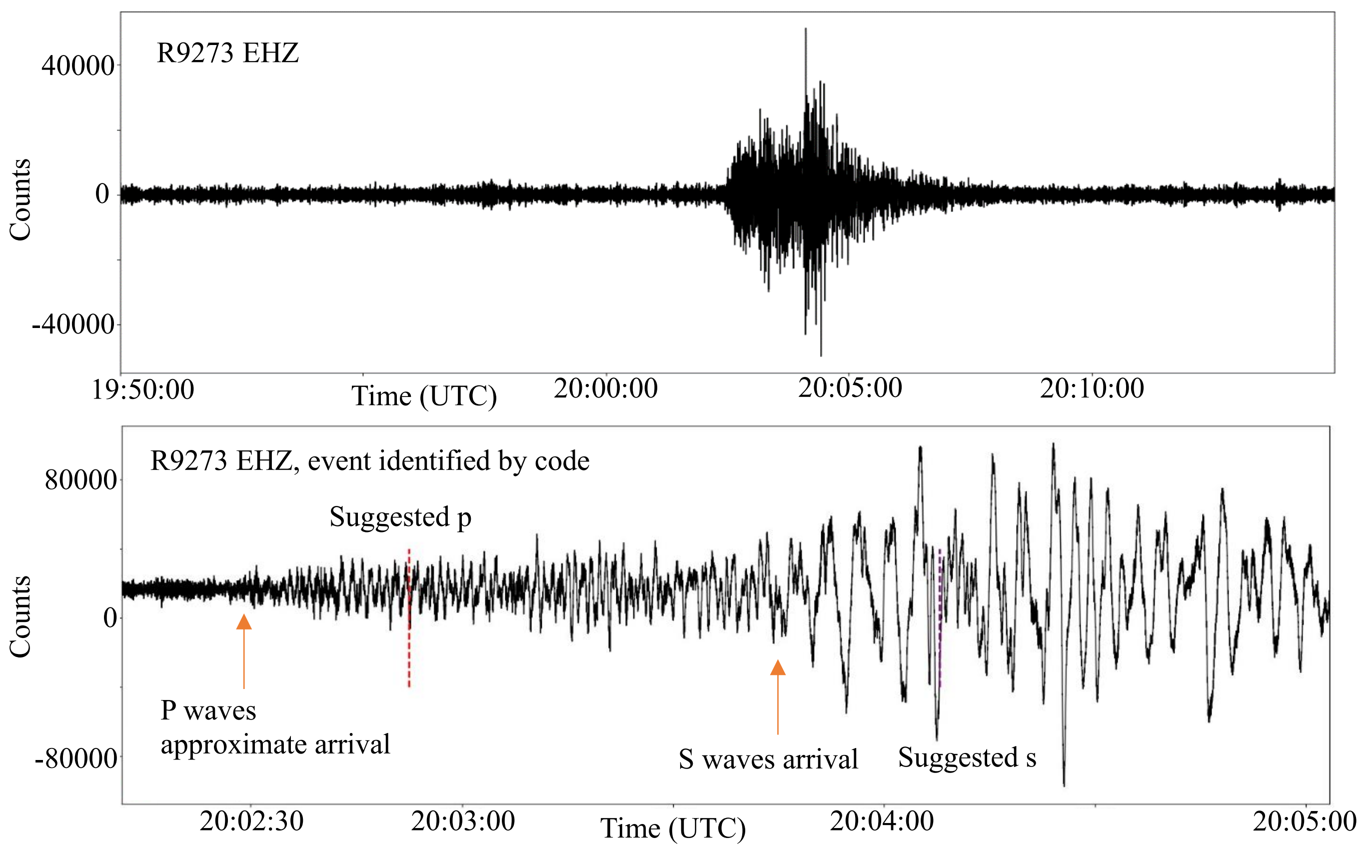

Figure 11. Counts plot for R9273 EHZ on Sumatra Event. In the second plot, the counts are shifted upwards due to filtering properties of the p-s picker function and an augmentation process that follows.

Just by looking at the counts plot, the p wave becomes difficult to detect over the night noise (fig.11 down). The spectrograms help with this. But this example shows how noise usually covers most of the information that is needed. It also explains the difficulty of the code in marking the waves' arrivals. The p wave seems to arrive at 20:02:27 (fig.12), while the s wave can be seen to arrive from fig.11 lower plot at 20:03:42 for a total distance of 630km from the epicentre (by multiplying times 8.4). This result is very close to the actual approximate 629km to the epicentre distance from this detector.

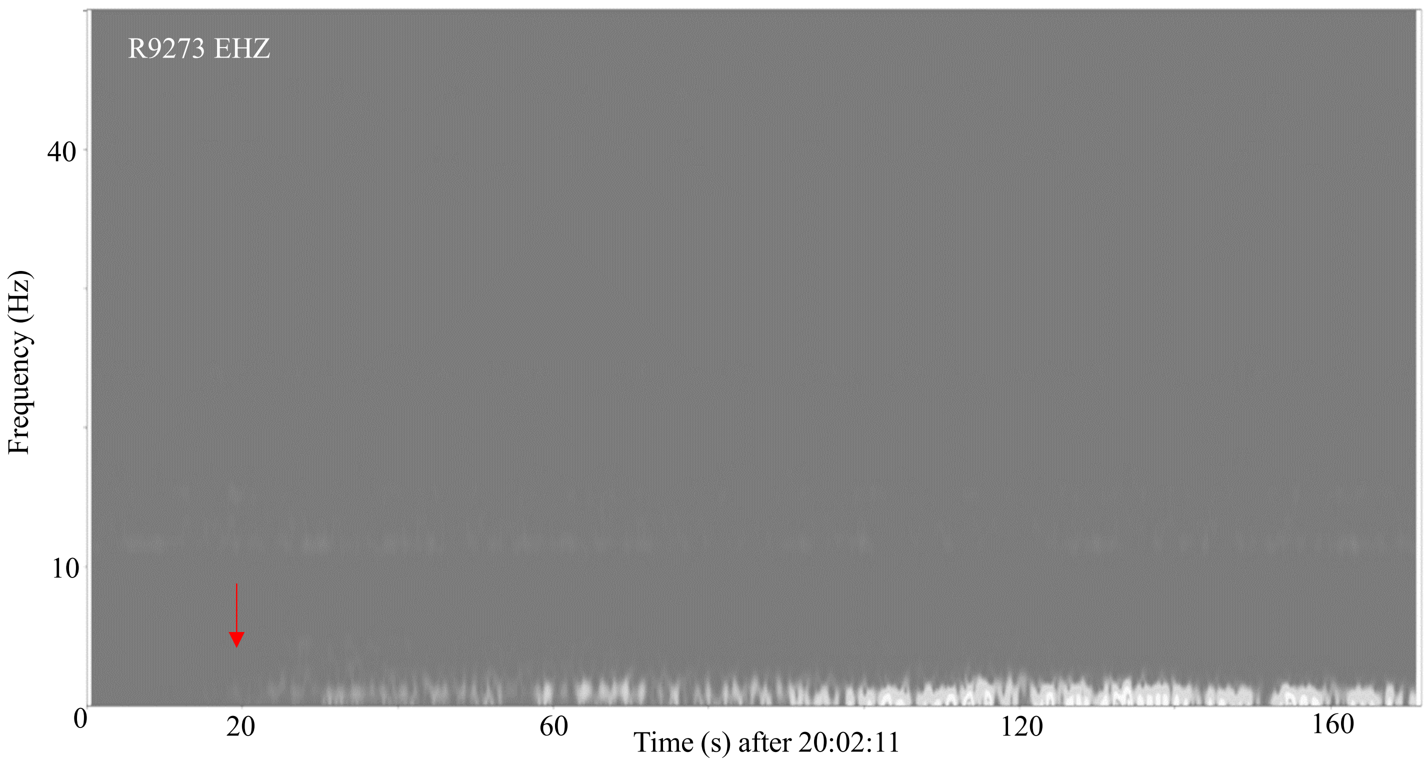

Figure 12. Spectrogram for R9273 EHZ for Sumatra Event. A zoom in on the plot shows that whiter colour indicates the arrival of the p waves on the low frequencies under 5Hz (red arrow).

On this spectrogram, however, notice how other higher frequencies start to appear too (around 10Hz). This indicates that R9273 is more susceptible to noise than BESC. This was the reason why in fig.6 (section 2.1.2), BESC was chosen to be the detector to which compare the others.

Repeating the procedure on the KAPK detector would give us the possibility to determine the origin of the earthquake. But, this would not be perfectly accurate as there is no way to realistically account for depth with this method.

All in all, the Sumatra earthquake is a good example of the program correctly identifying the earthquake given a full night of data for analysis. It also shows how the code plots the corresponding necessary data for later manual more exact interpretation. However, this is a very particular event as the strength of the earthquake was very high and occurred during nighttime and close to the detectors.

2.2.2. Case 2. Strong event during daytime.

The code was also tested with strong events during daytime. The main difficulty of this code is, nevertheless, filtering the noise caused by trucks and the inconsistency in the data collected by the seismographs. The next earthquake was a magnitude 7 that occurred in Java (IRIS ID 11688428) during daytime on the 14th of April.

When performing this daytime analysis, the event is going to be very difficult to distinguish from the background noise. As a result, a parameter of the code that only activates the z-detect function is enabled. The reason for this is that the carl-sta and sta-lta functions won't work as intended for the BESC and KAPK detector under these noise conditions, that is why they must be deactivated.

From the results, the code can detect the event and separate it from the background noise. It will also try to guess the time of arrival of the waves and plot the results for BESC and R9273 detectors, while it gives an error in plotting the KAPK detector. This error can be ignored, and it is due to the noise and lack of sensitivity of the KAPK detector on this specific date. Further analysis could now be done by the user on determining the earthquake epicentre as the p waves can be detected in the spectrogram and the s waves can be seen from the counts plot in the BESC channel EHN. But we will focus on the R9273 detector to show the difficulty of this task in some of these situations and showcase why the code is needed.

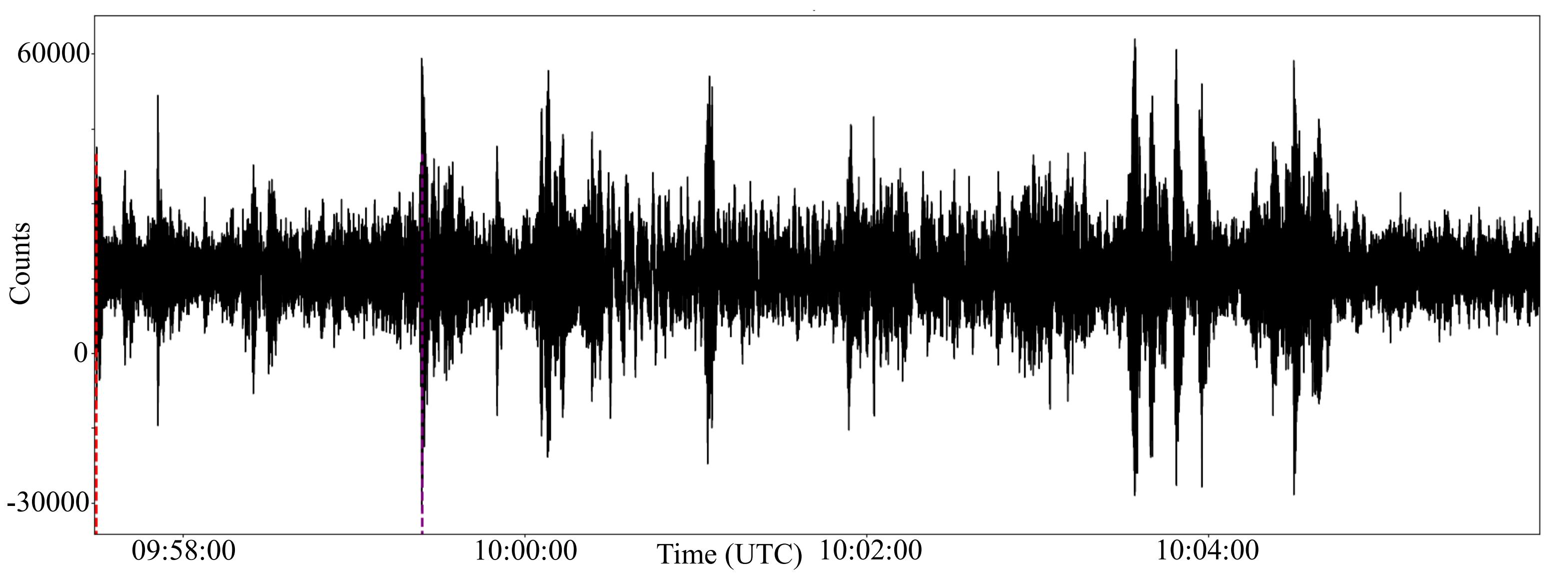

Figure 13. Data selected by the code from R9273 EHZ for the Java event. Notice how on the counts plot, the event cannot be separated from background noise, and the p and s waves picked by the code (red and purple lines) are incorrect.

The code was successful as this event was the only event plotted even though it was of same magnitude as other human made noises, showing that the correlation between detectors works properly. The p and s wave guesses made by the computer are, however, very wrong (as expected as the noise is too high) which can be better seen in fig.13, where the event is completely indistinguishable from the background.

In this noisy case, the p and s waves selected by the code should be ignored. Due to the high-background noise, it will be impossible for us to pick the s waves arrival with precision. The spectrogram, however, can let us precisely detect the p waves arrival.

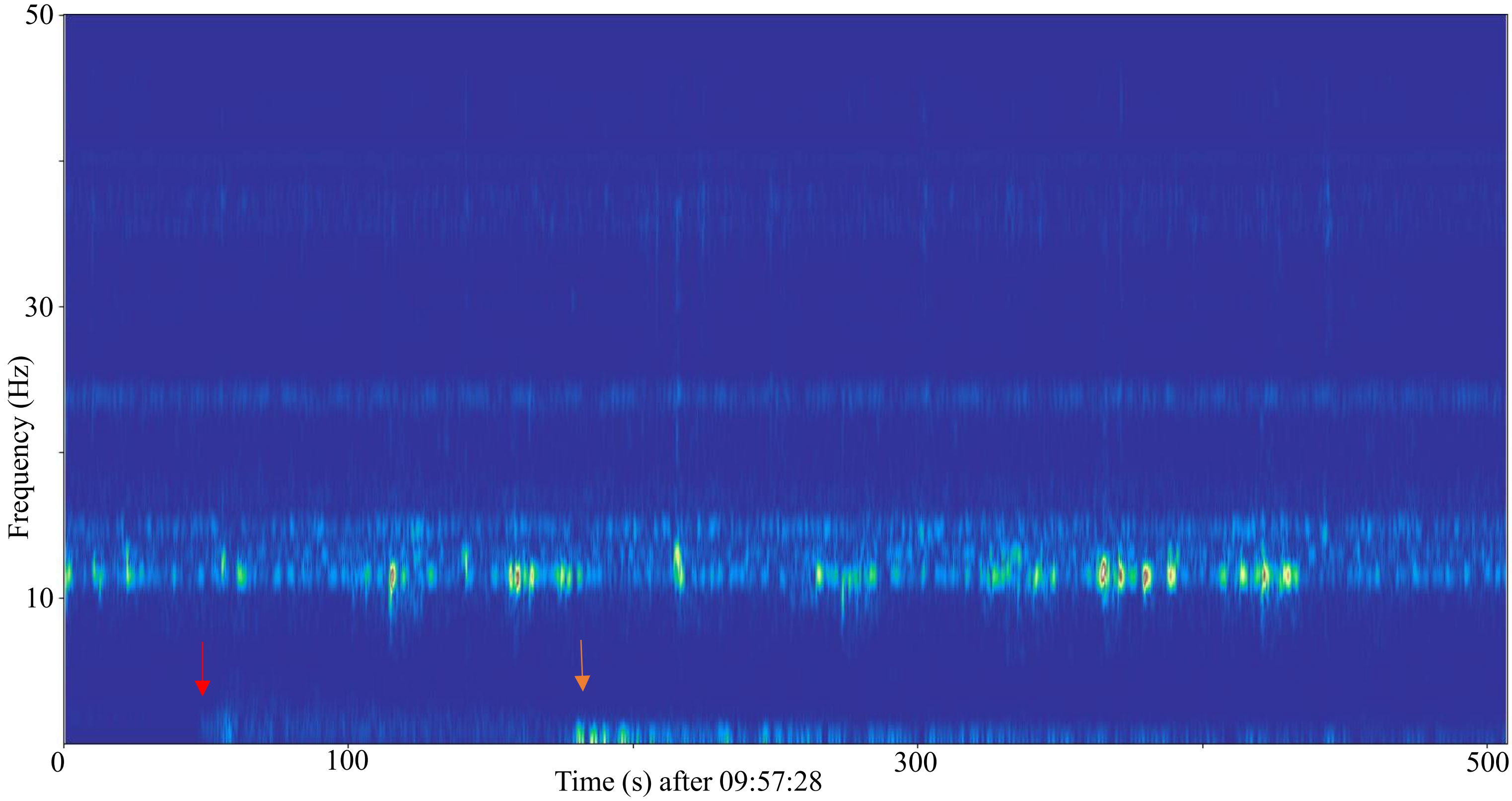

Figure 14. Data selected by the code from R9273 EHZ for the Java event. The p waves arrival is detected (red arrow). But the s waves arrival is not that clear as in the frequency spectrum these waves mix with the p waves and other surface waves. (Higher intensity frequencies in lighter colours)

Notice also how, approximately a hundred seconds after the p waves arrival, the rest of the waves will arrive with much more intensity (orange arrow). We are not, however, able to clearly separate the s waves from the earthquake surfaces waves with this technique, as some of these waves have very similar speeds.

Overall, this example shows how the code is successful in detecting events over extremely noisy environments where the human analysis becomes incapable of doing so. The code correctly analyses the daytime period and just picks this event by making use of comparisons between all the detectors. It then provides the user with the spectrogram and approximate times for later analysis. This spectrogram on velocity data analysis technique will be extremely helpful later as the fibre sensing project relies on detecting events in very noisy environments.

2.2.3. Case 3. Further strong event during daytime.

The program has also been tested for every event of magnitude over 6 after the Java earthquake until mid-June in addition to many other nearer smaller magnitude events. This was used to determine the detection capacities of the seismometers and to better understand what events we would be able to later see on the fibre sensing project. There are many examples, but some are shown next to better understand how the reader can separate noise from an actual earthquake based on the code plots.

On the 22nd of April a daytime Banda Sea event (IRIS ID 11686964) happened. The earthquake was originally of magnitude 6.2. The event was not isolated, as multiple smaller in magnitude earthquakes occurred simultaneously, some of which reached 5 in magnitude. The magnitudes of all these smaller events referred in the document are based on local magnitude scales (M_L)[13]. These scales are modified Richter scales that in this case consider the energy released by the earthquake. They are usually called Moment Magnitude (M_w) scales and determine how much work is done by the displacement of the rocks. This is calculated based on the known friction coefficient of the surfaces involved in the fracture or sliding that caused the earthquakes, as well as the displacement of those surfaces.

With the only z-detect function configuration and analysing a set of data around the Banda Sea earthquake, the code detects a total of 15 possible events. Most of them are just noise, which are discarded manually when looking at the spectrogram. Examples of these are the next.

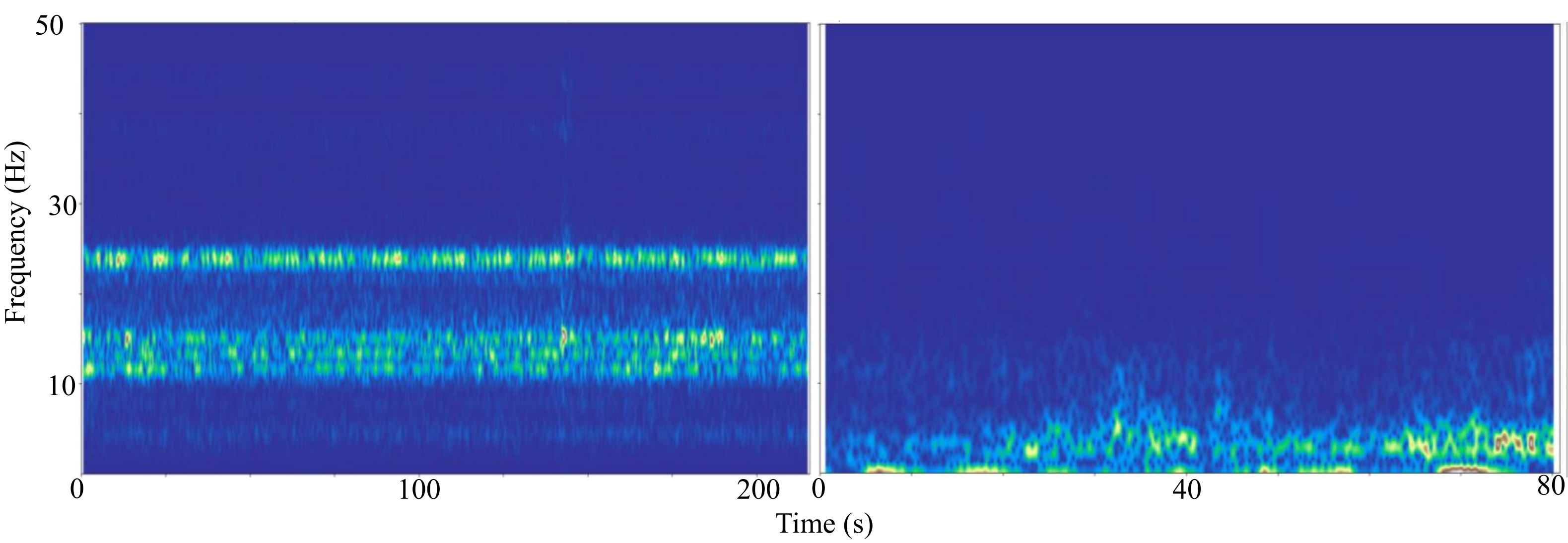

Figure 15. As well as the counts plots, the code also plots the spectrogram for each suggested event, which lets the user quickly discard between noise or earthquake. This are two of those suggested events that can be seen to be noise, as the usual earthquake pattern (sudden <4 Hz continuous break due to p waves arrival) does not appear on the low frequencies.

The regular counts plot does not provide much information on whether we are dealing with noise or earthquakes. However, the Banda Sea earthquake is noted in some of the suggested events by the code.

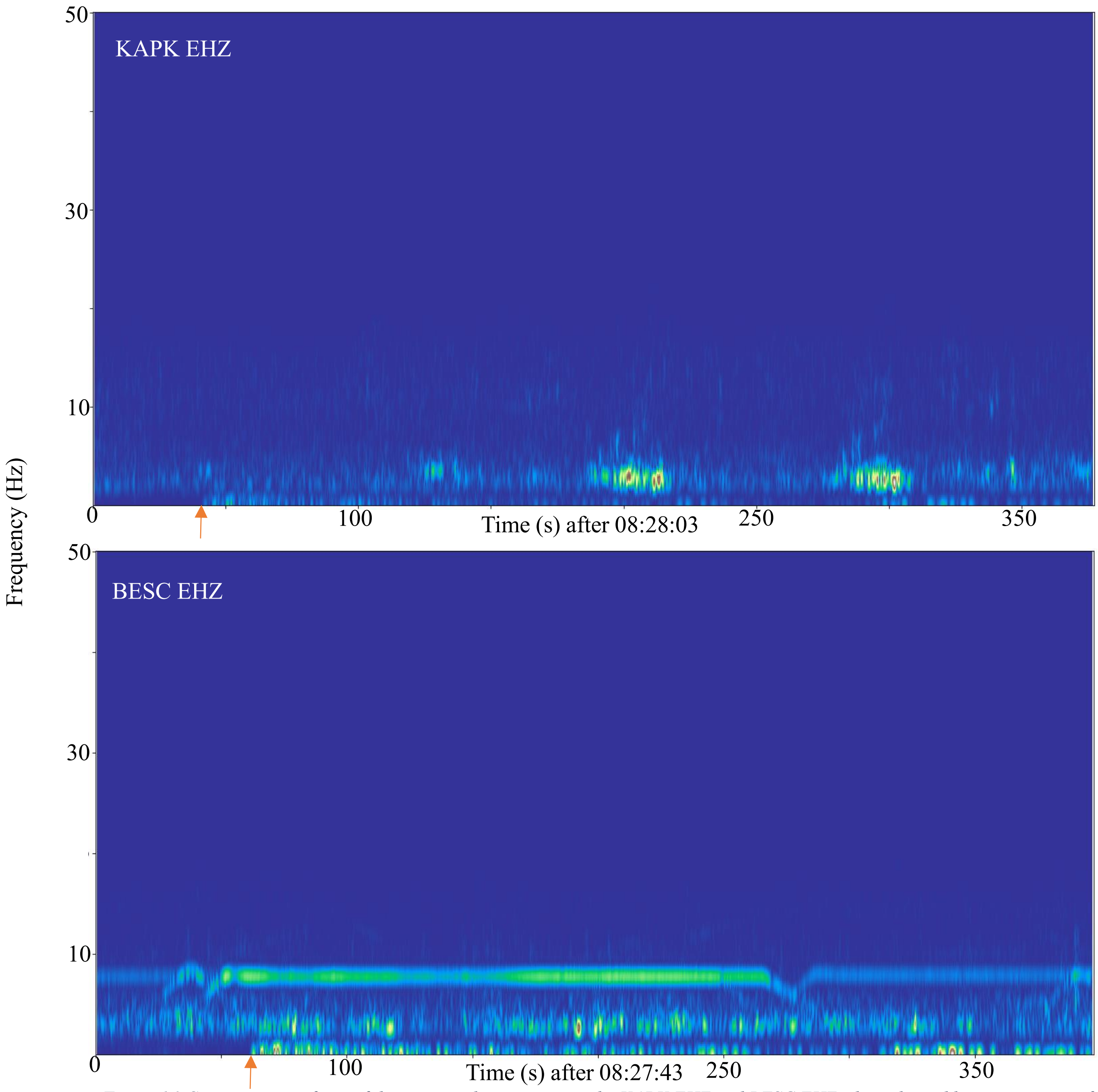

Figure 16. Spectrograms of one of the suggested events as seen by KAPK EHZ and BESC EHZ where the sudden appearance of the low frequencies indicated the arrival of an earthquake (orange arrow).

With spectrograms like those of fig.16, the p wave arrival on each detector becomes very clear. This example also shows how, when running the code on the just z-detect function, the code will over identify the number of possible events (unless a 7+ near event like Case 1 or 2 occurs). However, manual analysis can later easily check which of the suggested events are truly earthquakes and which are just noise, as can be seen with the comparison between the images of fig.15 and fig.16.

2.2.4. Case 4. Weaker and closer events.

Numerous sets of data were used to analyse the capacities of this code for events weaker in magnitude. The conclusions will be explained in the next section. But here a small remark must be made on the detection of earthquakes between 4 and 6 in magnitude at less than 1500km from Singapore. Most of the noise can be discarded with the spectrograms, however, it is much more difficult to distinguish from the global spectrogram the event from the noise.

The next is an example of the 2 of June earthquake in Northern Sumatra (ID 11703433). The earthquake occurred 167km in depth during the evening and so it was very faint. The next plot shows the difficulties of identifying the event from the spectrogram and why the combination of code plus user interpreting is needed for a successful result (which will be needed later on the fibre sensing data too).

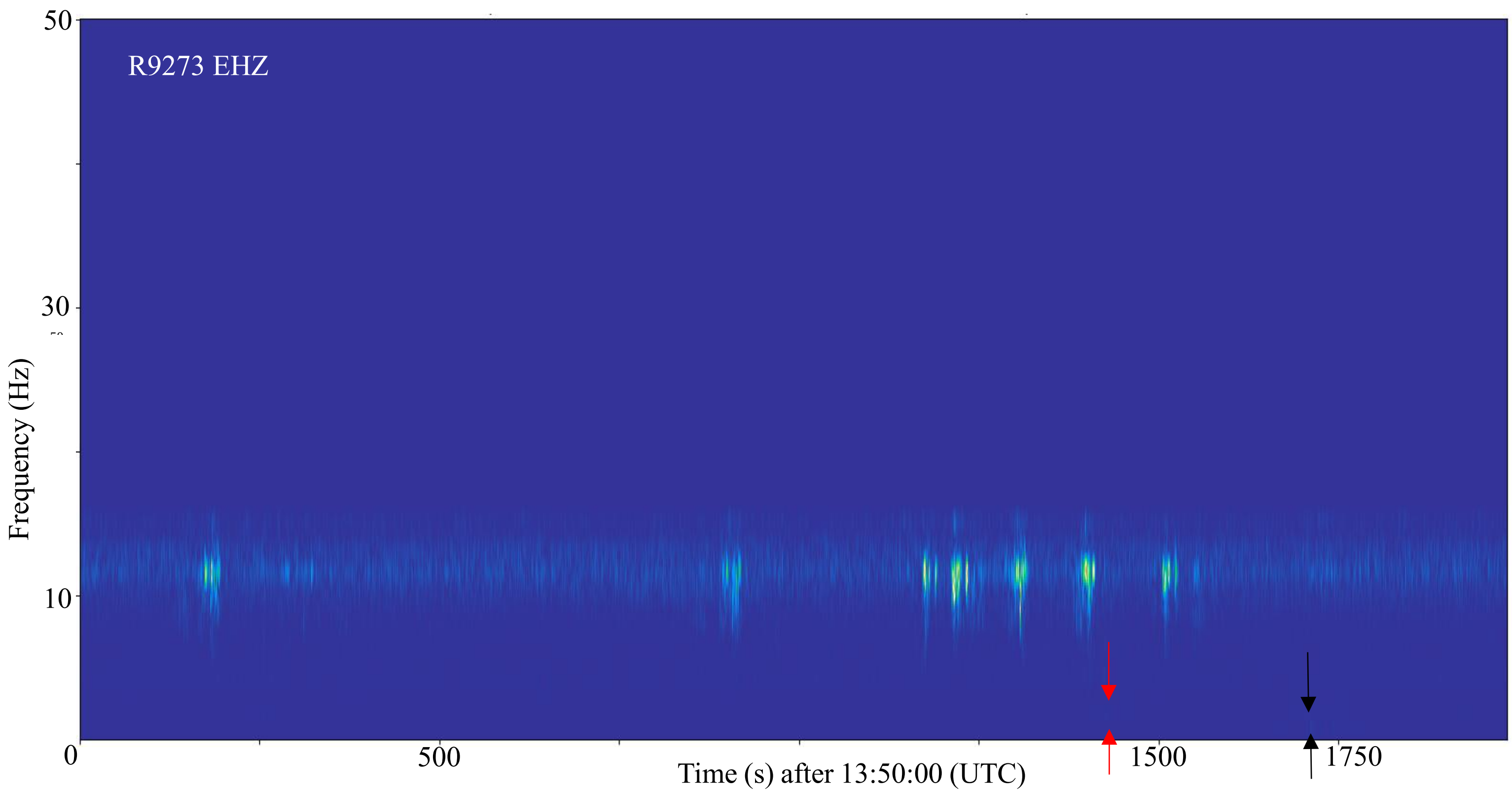

Figure 17. Global spectrogram of 33 minutes around the event. Recall that earthquake events appear in the smaller than 10Hz domain.

After carefully looking at the spectrogram (fig.17), on the less than 5Hz domain there seems to be a possible event a bit before 1500s (red arrow, but really faint). The next plot from the R9273 EHZ will show how this is in fact noise (fig.18A). This is noticed because the frequencies do not reach under the 1 Hz margin uniformly, like an earthquake would do. The actual 4.8 magnitude event (black arrow) is shown in the following plot (fig.18 B), where the frequencies domain does resemble that of a natural earthquake.

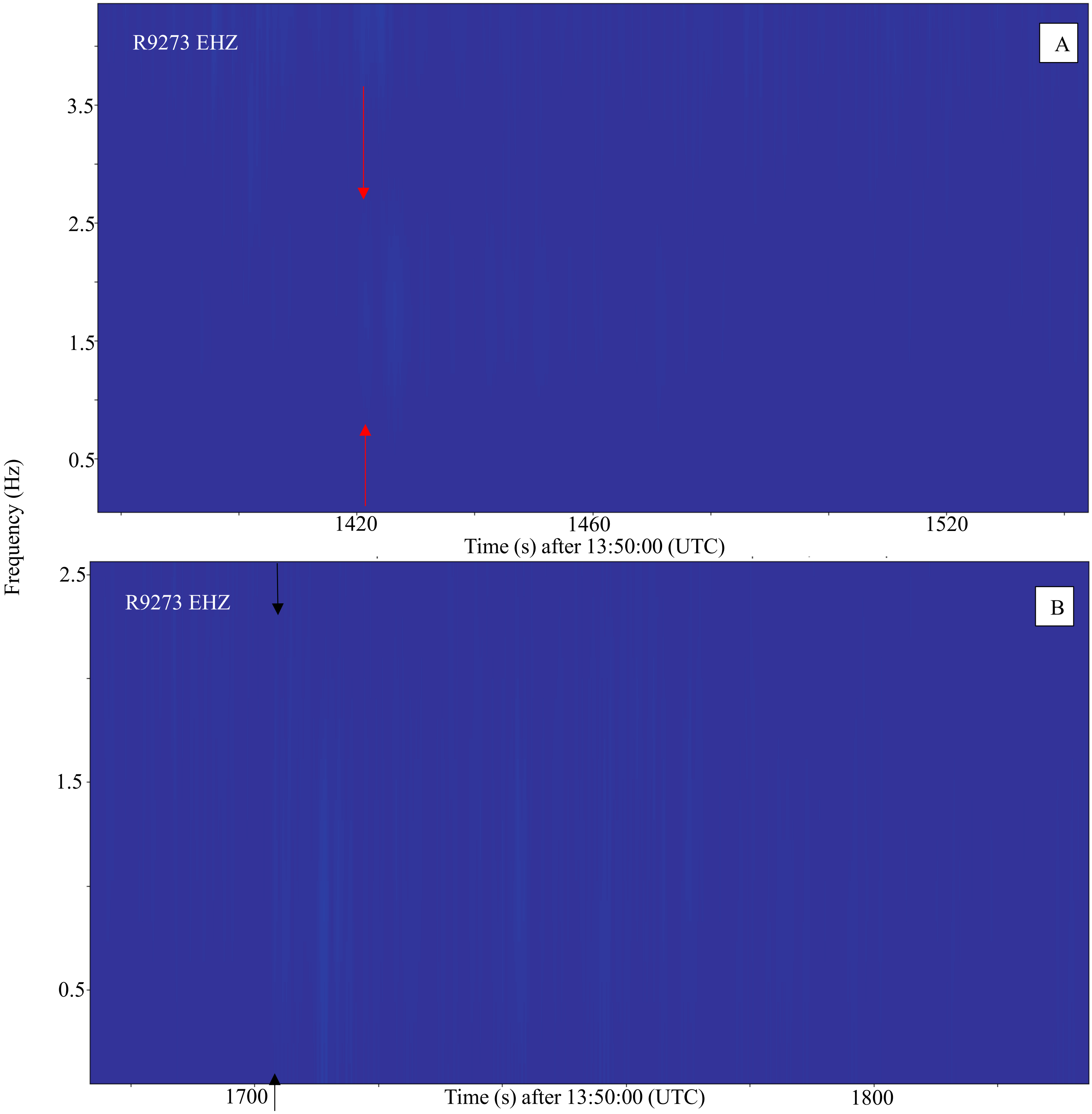

Figure 18. Plot A is the noise (red arrow from fig.17), while the B determines the arrival of the p waves (black arrow from fig.17) by the slight but sudden increase in the smaller than 1Hz frequencies.

The previous figures show R9273 EHZ detection of the event. To show that comparison between detectors is fundamental, we will now look at BESC EHZ, which is presumably more sensitive but noisier.

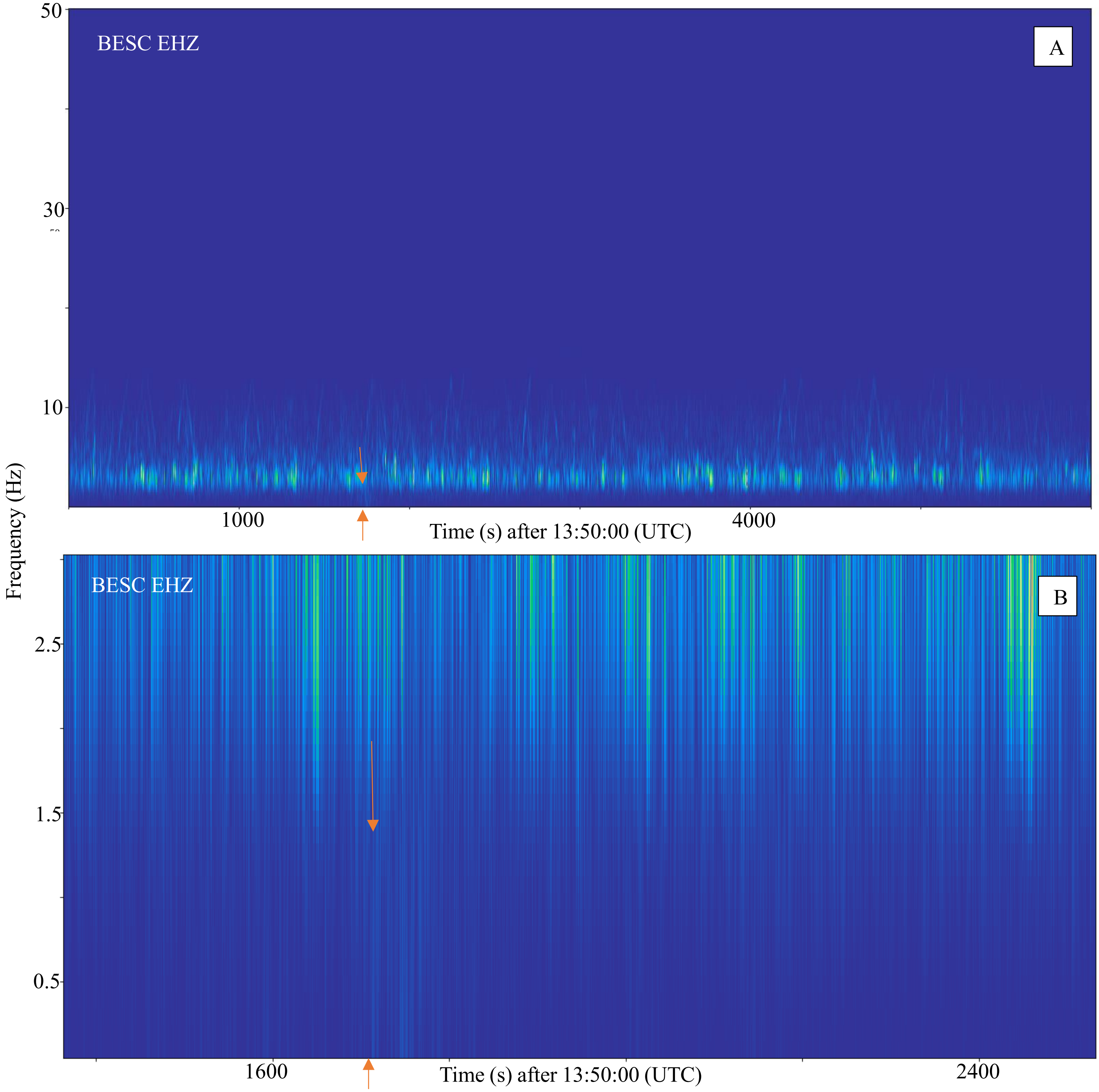

Figure 19. Global spectrogram (A) of the same event as fig.17. Zoom in on the spectrogram (B) where the first p waves can be seen arrive over the noise around the 1700s (orange arrow). This is the same detection than that of fig.18.B.

This also examples how the BESC EHZ detector is more sensitive as the arrival is clearer on the global spectrogram than that of R9273 (compare fig.17 with fig.19A), but the noise also occurs at lower frequencies on this detector.

Overall, the event was registered by the code and plotted (fig.20) between other possible events that correspond to noise, and that could be easily discarded by the user using the spectrograms. Figure 20 is the actual event as suggested by the code. The user can then confirm it to be an earthquake. This example showcases the difficulty of detecting small events but helps to expand on the techniques later used on the fibre, where noise levels are expected to be high. In conclusion, from the velocity plot nothing can be seen, but deeper analysis on the spectrogram can precisely give information on the arrival of the waves.

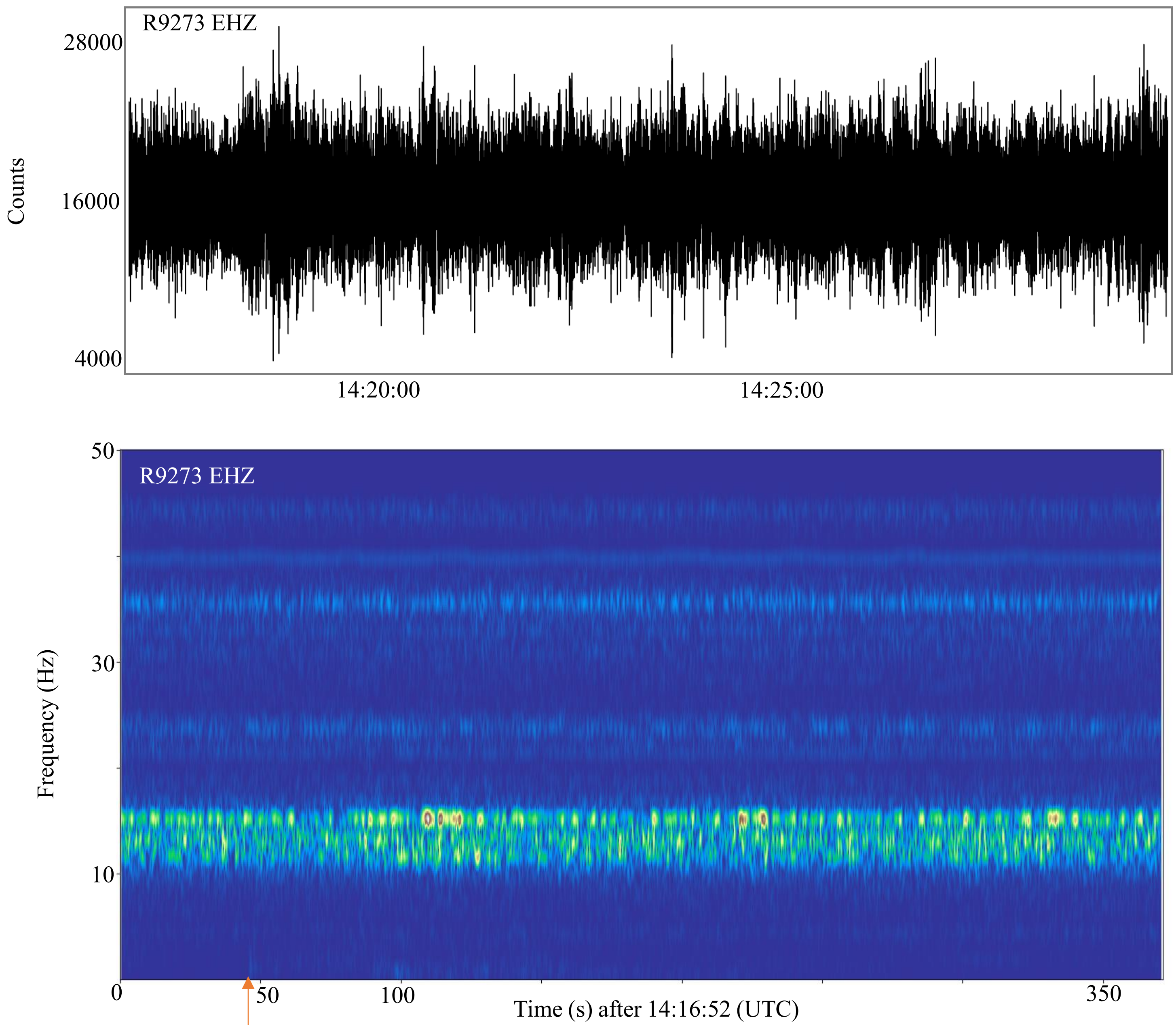

Figure 20. The suggested as possible event by the code that we manually identify as the earthquake by the arrival of the low frequencies just before the 50s mark (orange arrow). These are the plots given by the code that correspond to the manual analysis we did on the fig.16 and fig.17. As can be seen from the counts plot (up), this event cannot be separated from the noise and so the s waves cannot be registered.

2.3. Conclusion on effectiveness of the code

Finally, we can make some approximations on the detection capacities of the code and seismometers based on the many events tested. The next table summarizes it. On it, automatic means the code just separates from the noise, while automatic + manual means that some suggestions will be made, and the user has to pick which ones are valid (Case 3) or directly look at the global spectrogram (Case 4).

<table>
<tr><td>DETECTIONS TESTED</td><td>Up to 1000km</td><td>Up to 4000km</td><td>Up to 8000km</td></tr>
<tr><td rowspan="2">Day</td><td>6.5+ automatic</td><td rowspan="2">Variable, usually 5.5+ automatic + manual</td><td rowspan="2">Variable, usually 6.5+ automatic + manual</td></tr>
<tr><td>5+ automatic + manual</td></tr>
<tr><td rowspan="2">Night</td><td>6+ automatic</td><td rowspan="2">Variable, usually 5+ automatic + manual</td><td rowspan="2">Variable, usually 6+ automatic + manual</td></tr>
<tr><td>4.5+ automatic + manual</td></tr>
</table>

Table 1. Approximate tested capacities of the code to register earthquakes of a given magnitude at a certain distance from the detector.

The higher limits are very approximate as events as far as 300km south of the coast of Tonga Islands (more than 9000km away from Singapore) have been clearly distinguished on the spectrograms if they are 7+ in magnitude. While events of less magnitude cannot be seen at those distances. Also, these values are a general approximation as it all depends on the specific noise levels on a day or the state of the seismometers. Similarly, events of less than magnitude 4 are also sometimes manually observed using spectrograms.

Much of the variability on the results as well as the need for manual confirmation is due to R9F0D not being a very good detector, and because of the need for confirmation of at least BESC and another detector. This necessity makes it very hard for an event to be registered if there is constant daily noise in any of the three main detectors.

Overall, the main conclusion is that the spectrogram is the most useful tool given by this code. The code can help with the detection but is looking at the spectrograms of the suggested events by the program what gives the most information to the user. Furthermore, now that we can precisely determine when earthquake waves arrive to NUS, we can use the techniques described here on the fibre sensing project.

3. Fibre sensing setup

The Michelson interferometer setup could have provided us a phase value that would have been related to length changes in the sensing fibre (section 1.2). However, those length changes would have been ambiguous when the power output from the photodiode was on its maximum or its minimum. To solve this, and heterodyne phasemeter is used. This section will explain the phasemeter setup and the demodulation step needed to obtain the phase measurement.

In addition, the section will cover some of the early noise measurements observed in the phase reconstruction and the steps taken to solve them.

3.1. Heterodyne phasemeter

For our setup we use a Thorlabs SFL1550S laser. This laser operates at a wavelength of $\lambda = 1550$ nm (commercial optical fibre wavelength) and provides an output power of 5mW.

To solve the ambiguity issue, the set up will add to the Michelson interferometer an acousto-optic modulator, or AOM (Brimrose, AMF-80-20-1550). Particularly, we use a driving frequency of $f_{AOM} = 70$ MHz and so an angular velocity of $\Omega = 2\pi f_{AOM}$. The AOM, installed on the shorter arm before the Faraday mirror, will add this frequency to the light on this path on the way to the rotator and back from it, for a total angular velocity of $\omega_1 = \omega + 2\Omega$ while $\omega_2 = \omega$ stays the same.

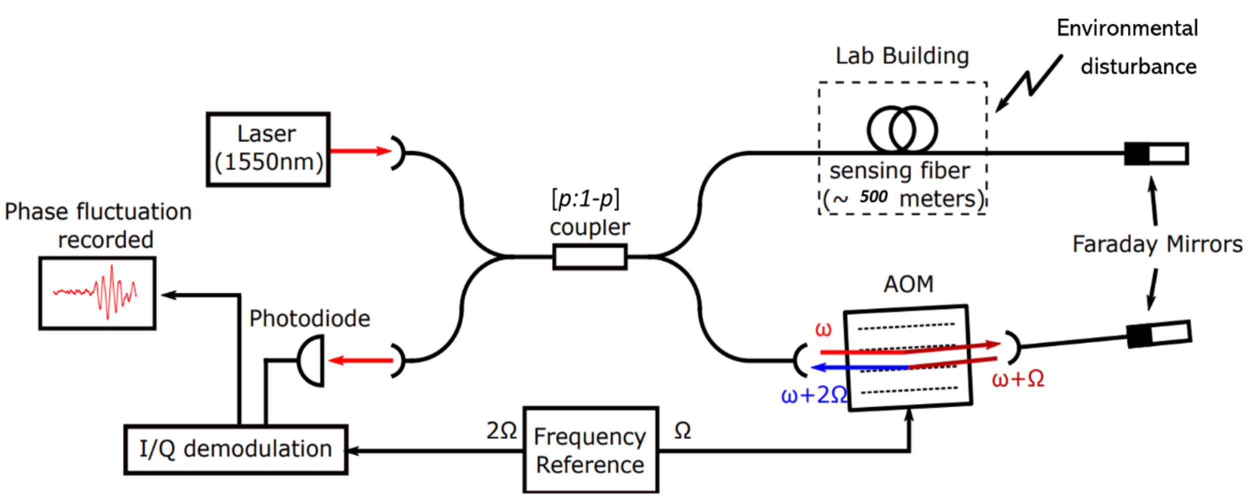

Figure 21. Diagram of the experiment phasemeter description.

Similarly, as before, we can now analyse the power and electric field out from the interferometer:

$$E_{out}(t) = \frac{E_{in}}{2} e^{i(\omega_1 t - k2L_1)} + \frac{E_{in}}{2} e^{i(\omega_2 t - k2L_2)} = \frac{E_{in}}{2} e^{i(\omega t - k2L_1)} (e^{i2\Omega t} + e^{-ik2\Delta L})$$

(6)

Now, we can simplify using the phase difference angle θ from the introduction:

$$E_{out}(t) = \frac{E_{in}}{2} e^{i(\omega t - \theta - k2L_1)} (1 + e^{i2\Omega t + \theta})$$

(7)

By taking the complex square and simplifying we will get the output power:

$$P_{out}(t) = \frac{P_{in}}{2} (1 + cos(\theta + 2\Omega t))$$

(8)

As can be seen, a beat signal appears, with a frequency $f_{beat} = \frac{2\Omega}{2\pi}$. This beat will be detected with the fast InGaAs (Indium Gallium Arsenide) photodiode (we used the model GPD GAP100FC). The length change information has been modulated into the observable signal. Now, a demodulation process must be followed to obtain the phase θ information.

3.2. Demodulation

The process to obtain the phase will consist of an I/Q demodulation. In our case, we use a digital demodulator [4]. The idea is to use a strong signal, a local oscillator, at $2f_{AOM} = 140\ MHz$. This signal is divided into two, one of them delayed to the other by π/2. With this, we will have a $cos(2\Omega t)$ and $sin(2\Omega t)$ strong signals. Now, we will multiply the incoming signal of the P_{out} from the photodiode with each.

$$P_{out}(t) \cdot cos(2\Omega t) = \frac{P_{in}}{2} (2cos(2\Omega t) + cos(4\Omega t + \theta) + cos(\theta))$$

(9)

$$P_{out}(t) \cdot sin(2\Omega t) = \frac{P_{in}}{2} (2sin(2\Omega t) + sin(4\Omega t + \theta) - sin(\theta))$$

(10)

By applying a low-pass filter to each signal, we can get rid of the higher frequency terms (2Ω and 4Ω). Operating the remaining signals, which we refer as I and Q, we can get the desired phase θ.

$$I = \frac{P_{in}}{2} cos(\theta)$$

(11)

$$Q = \frac{-P_{in}}{2} sin(\theta)$$

(12)

And so finally:

$$\theta = \tan^{-1}(-Q/I)$$

(13)

Once we have this phase difference, which does not have the problems raised by the Michelson interferometer, we can use the initial $\theta = k2\Delta L$. With this relation, it is clear than any changes in the phase will correspond to a change in the difference in length between both paths. Therefore, as the short path is significantly shorter than the longer one, this can be interpreted as the longer fibre having been disturbed. With this idea in mind, we will later analyse the data from this phase reconstruction measurements in the hope of detecting any events.

3.3. Noise in the phase reconstruction

Before being able to apply the code and techniques to the data of the fibre sensing project, work had to be done as the phase reconstruction information was too noisy. In this section, the noise that initially appeared on the phase reconstruction of the laser and its possible causes will be identified. Some of the implemented solutions will also be shown.

3.3.1. Early noise measurements

Initaially, the noise on the phase reconstruction was measured and compared with that of the voltage at other points in the experiment setup, trying to find some relationship.

The noise observed in the phase reconstruction as of mid-June 2023 will be shown next (fig.22). The set up was a 1550.056nm laser with 2MHz sampling in a 500m fibre (and so a total 1 km path difference) and 566.7 mA current input into the laser. The phase seems extremely irregular (fig.22). If we zoom in (fig.23), we will observe a constant ±2.5π vertical error in 1/2π units. This error is large enough to hide any possible measurement as the phase variations due to length changes (ΔL from the introduction) on the 500m fibre are not expected to be more than a few units (chapter 4.2).

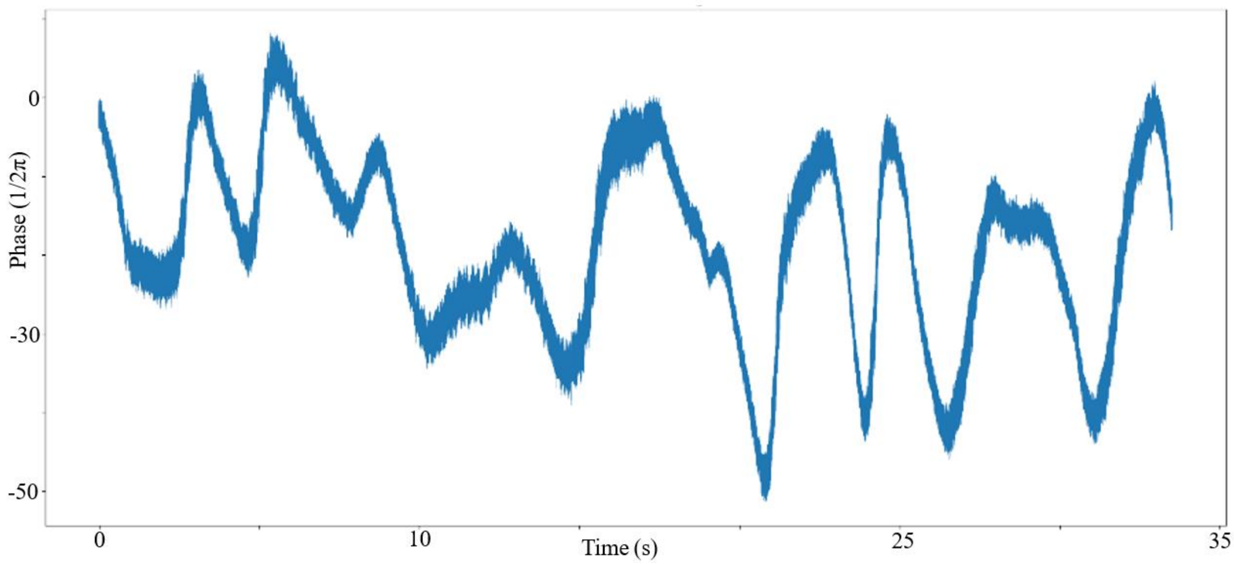

Figure 22. Plot of the phase reconstruction data with respect to time. The phase represents θ/2π from the introduction.

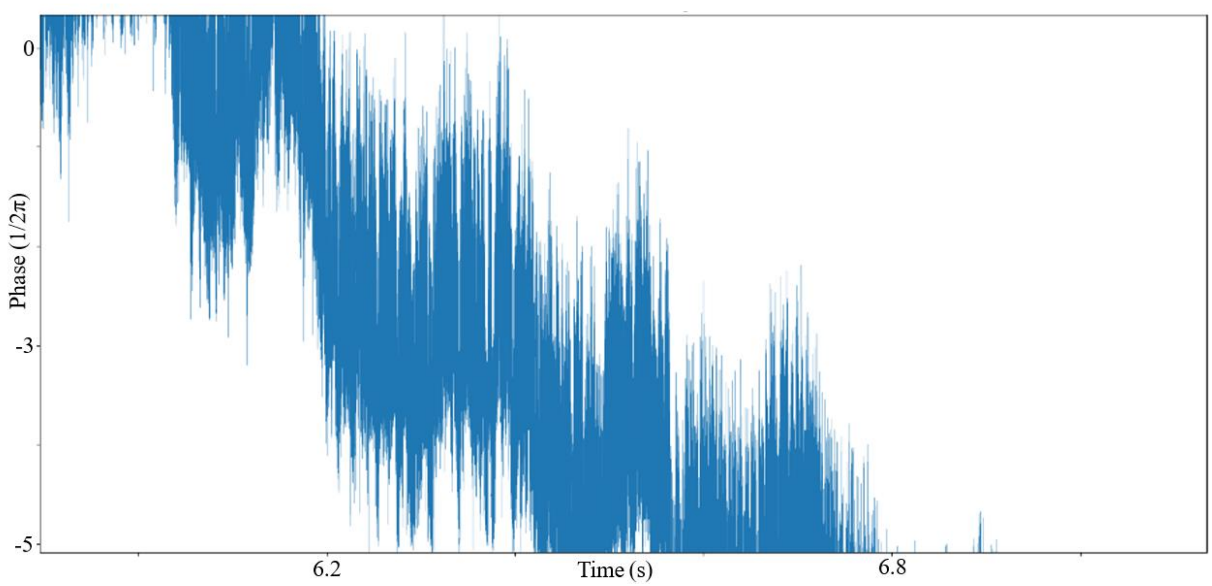

Figure 23. Zoom in on Figure 22 where the vertical 2.5 displacement can be observed.

By applying FFT to this measurement and others, the frequencies of the noises in the phase reconstruction were obtained and are classified (fig.24).

A similar process is now repeated using voltage measurements for an identical experiment set up. Using a spectrum analyser, the noise at different places in the experiment was registered. Of special interest was the measurements of the driving frequencies in the signal from the local oscillator (LO) to the AOM. A bad signal here would cause the 2Ω in the shorter arm to not be exact and could be generating the noise issues. Before reaching the AOM however, the signal goes through a lowpass filter and an amplifier. For this, measurements of the signal before and after the amplifier were also done.

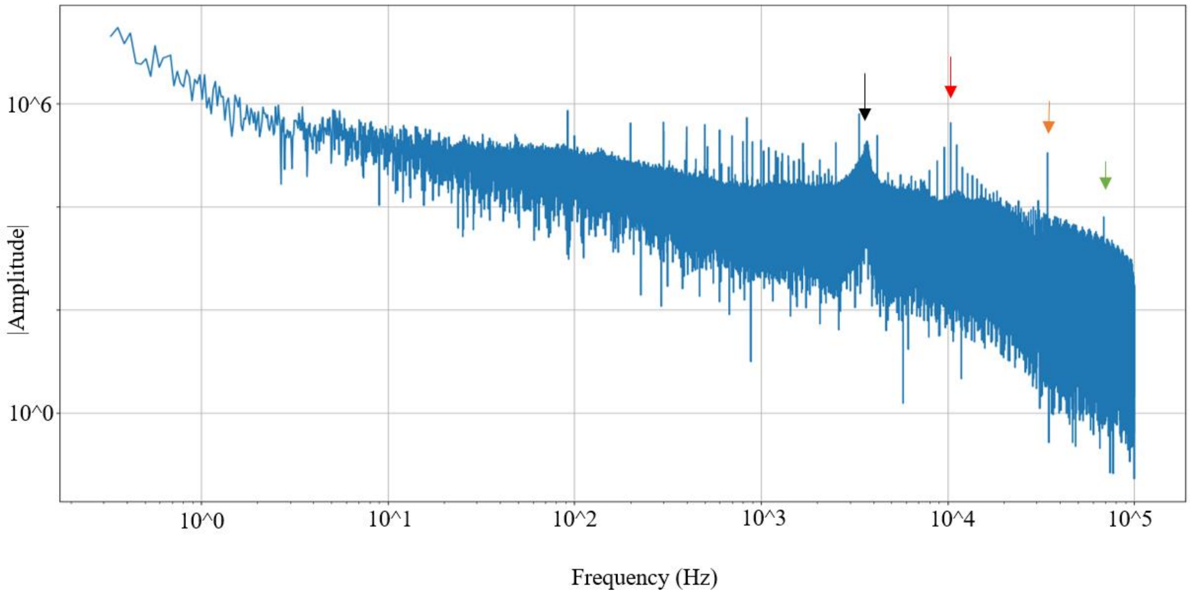

Figure 22. Frequencies obtained by FFT from the phase reconstruction. The arrows mark the most relevant noises.

The tables of all these noise frequency results are not included in this document for brevity. But the main conclusions are described next.

3.3.2. Early conclusions

It is important to first note that the frequencies at which noise is seen on the phase reconstruction fig.24 should not be directly related to those measured at other steps in the experiment, as they correspond to different physical observables. However, some noise in the phase seems to occur in recurrent frequencies.

At 3.7 kHz, a wide peak (black arrow) is seen on almost every measurement (both voltage and phase). This recurrence might indicate it is related to the laser. In addition, a 10.4 kHz (red arrow) measurement just seems to appear only on the phase. It has side bands every exactly 0.8 kHz and it is centred at precisely 10.400 kHz, which might indicate that it comes from the demodulation step and it's not an external noise. There is also noise at 34.434 kHz (orange arrow) which seems laser or current related.

Furthermore, a frequency that must be taken into consideration is at 78.2 kHz, where a wide peak appears only on the measurement after the amplifier before the AOM.

3.3.3. Solution attempts and observations

The main solution attempt was adding filters directly to the laser and the signal from the LO to the AOM. The AOM initial low pass filter had some parts that were damaged replaced and an extra bandpass was included after it (and before the amplifier) for extra filtering. Also, a similar noise in the frequencies as that observed at 3.7 kHz was found in the laser fabrication manual. The attempted solution to reduce it was changing the configuration driving the laser from 566.7 mA to 382.5 mA. This last change and the filters implementation seemed to overall get rid of much of the noise in the lower frequencies in the phase reconstruction. It also eliminated the 34 kHz noise and 68 kHz noise (green arrow on fig.24) seen on the phase. The 10.4kHz noise remained there which supports the idea that it may be originated in the demodulation step.

With these changes, the vertical error on the 500m fibre was reduced from $\pm 2.5 \cdot 1/2\pi$ to $\pm 0.1 \cdot 1/2\pi$. This achievement opened the door to earthquake detection.

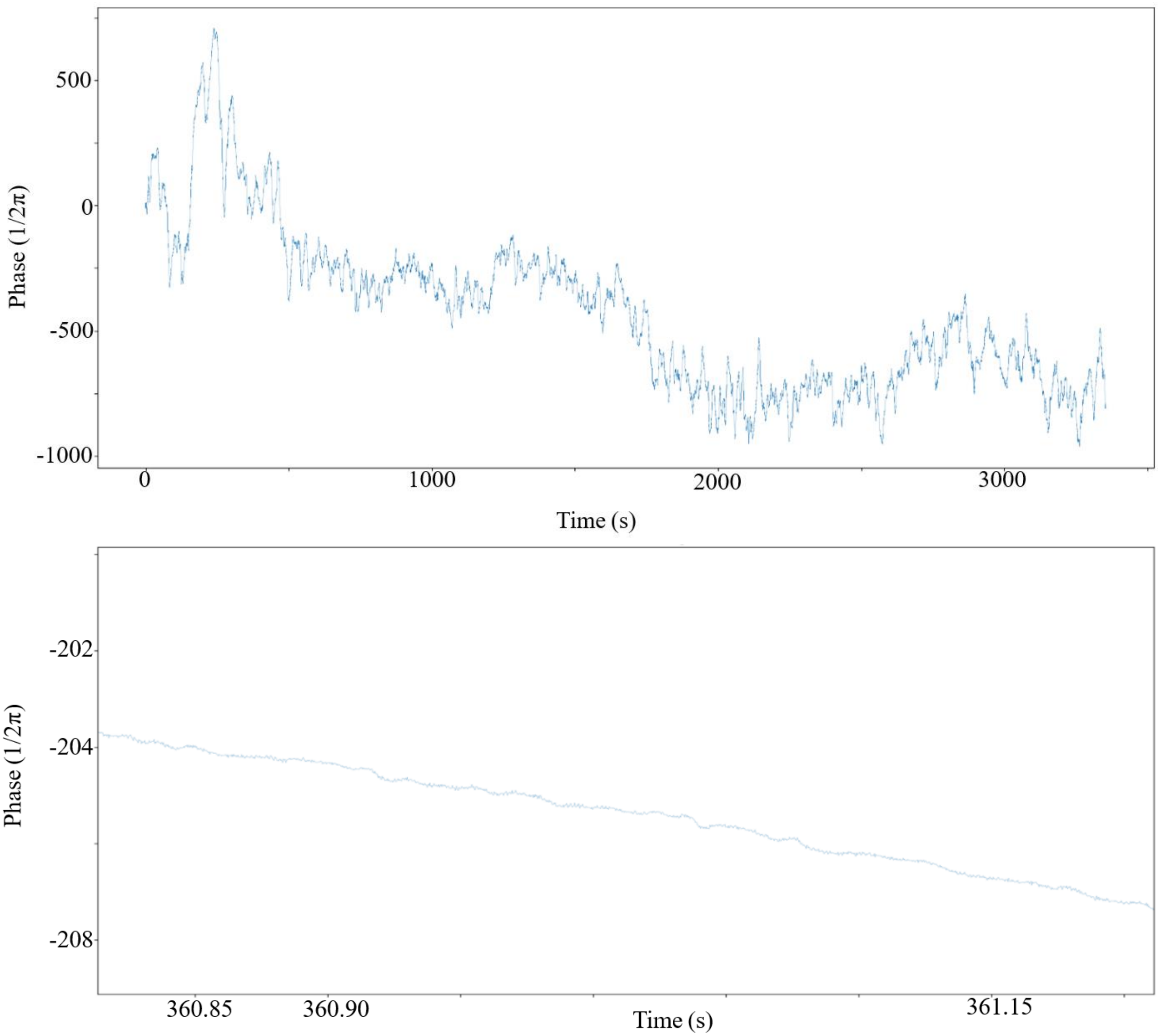

Figure 23. Plots from measurements with the new set up. The vertical error can be observed to be not more than 0.1 while the overall phase fluctuates without constantly increasing which would have indicated a problem in the configuration.

4. Detections with fibre sensing

With the new setup, the sensitivity of the experiment is much better than before. It seems it is even able pick acoustic signals, as weak as human voice one meter away from the fibre (with 2 MHz sampling rate). However, for the long-term analysis of the data, the 20 kHz sampling will be used for the sake of storage capacities and because seismometers operate at an even lower sampling rate.

4.1. Noise in the phase and velocity

Even though the measurements now seem to have a lower noise base, there is still some noise pattern that repeats itself and that can be better identified when looking at the spectrogram. The spectrogram is that of the velocity, obtained by a linear approximation on the phase data.

Remember from the introduction that:

$$\theta = k2\Delta L \ , \qquad \Delta L = \frac{\theta}{2k} = \frac{\theta\lambda_0}{4\pi n}$$

(14)

And so, by taking consecutive points of data then:

$$v_i \ \approx \frac{\Delta L}{\Delta t} = \frac{\left(\frac{\theta_{i+1}}{2\pi} - \frac{\theta_i}{2\pi}\right)\cdot\lambda_0}{\left(\frac{1}{sampling\ rate}\right)} \cdot \frac{1}{2n}$$

(15)

Notice that what is being observed on the data (fig.25) is not exactly θ but rather θ/2π. By taking the taking the difference in the phase measurement (in 1/2π units) between two consecutive points and multiplying by the wavelength we get an approximate displacement of the fibres. If we divide this by the time in between each measurement (determined by the sampling rate), we can get our velocity.

However, this is not a regular velocity measurement. This quantity represents the rate at which the changes in the path difference occur, and so it is different to seismographs measurements, which directly record the velocity of the displacements caused by the earthquake. That is why we can disregard the 1/2n factor, as we are not interested in the value of this velocity but rather how the velocity at a point compares to that at other points.

Even if the velocities in the phase and in the seismographs represent different physical observables, the frequencies at which we expect some of the events to occur will be similar (this will be shown later in section 4.3). A spectrogram for noise analysis is presented next.

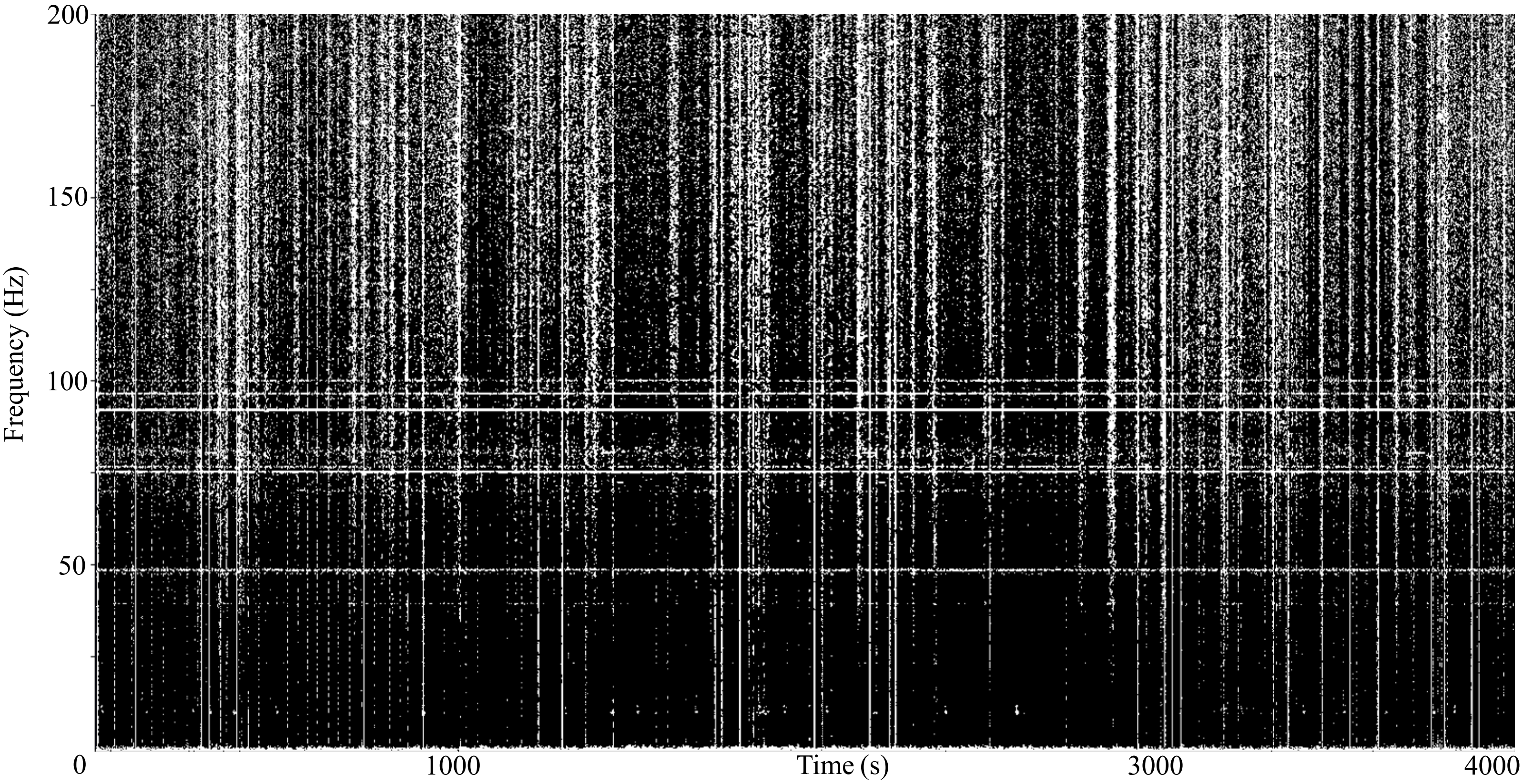

Figure 24. Spectrogram on the velocity approximation of a phase measurement with the new configuration on a 500m fibre. The whiter the colour, the more intensity in those frequencies.

The interpretation of Figure 26 first starts from the vertical lines. These lines indicate that there has been a significant vertical disruption in the phase. They are observed on every measurement performed. When looking at the phase plot, they correspond to mistakes in the phase reconstruction or laser instability. There seem to be three types of breaks that repeat often and that are the cause of these lines.

Type 1 will be defined to be the most common of them all (fig.27.A). On it we observe a short period phase break that may correspond to demodulation issues. On this first type, the break goes back to almost the original phase value. This error occurs every few tens of seconds without apparent pattern. Type 2 is very similar but less frequent. On this case the phase does not return to the original value (fig.27.B).

Finally, type 3 is a laser instability error that results in a vertical break after a consistently increase in oscillation (fig.27.C). This is the least common, but it holds the largest impact on longer fibres measurements as will be shown later.

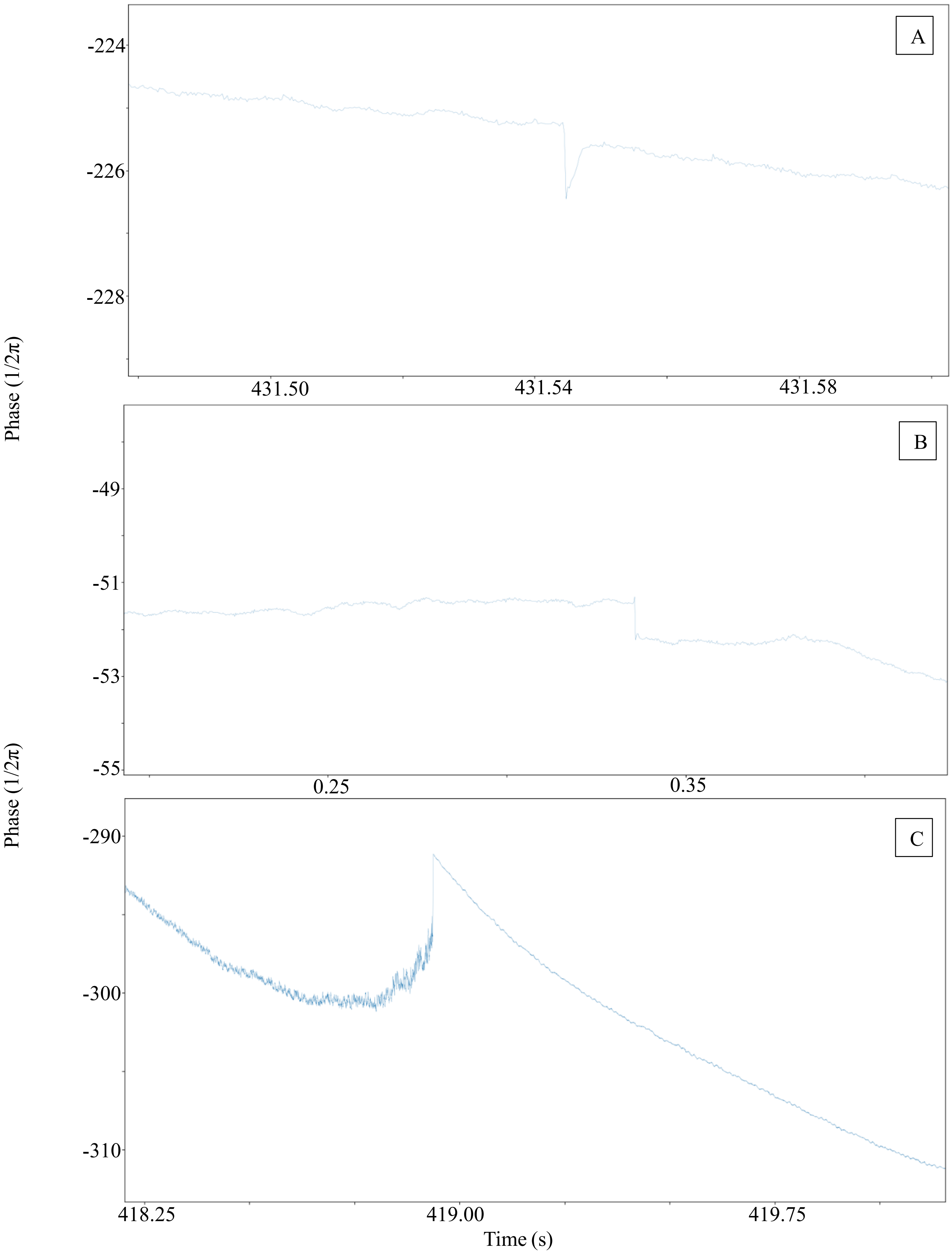

Figure 25. Errors in the phase measurement that cause the vertical lines seen in the spectrogram.

Leaving aside these errors, we next focus on the constant horizontal lines (fig.26). These most likely represent mechanical (acoustic) noise from the surrounding of the fibre. Some of them are seen on very specific frequencies that can be related to those of the ventilation of the labs. Most of these noises should disappear when the experiment is moved to an acoustic isolation room. Still, many of these frequencies should not be relevant for earthquake detection as they occur at very recognizable values and so they can be discarded with software. Some of the most noticeable recurrent noise is at 49 Hz, 73Hz and 98Hz. But the conflictive noise occurs at low frequencies, as there is a constant range under 1 Hz occupied by it that coincides with the range expected to find earthquakes on.

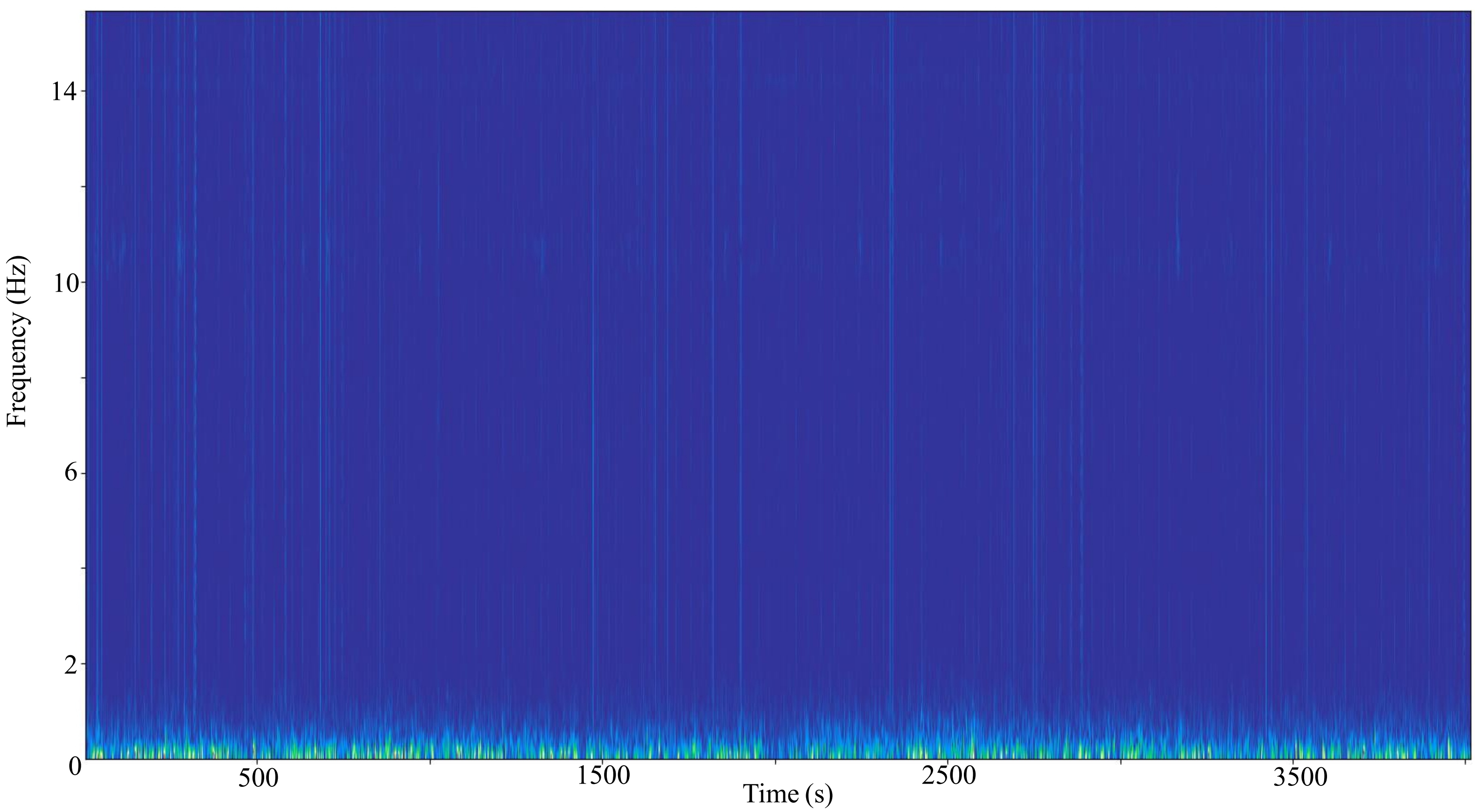

Figure 26. Noise on the spectrogram for the low frequencies on the 500m fibre measurements. The vertical lines correspond to the previously mentioned errors and difficult the detection of an event.

Having found at which frequencies the noises occur, we can now look for recognizable events.

4.2. Detections

The following are examples that verify that detections can be made. First, we will look at human made noises such as entering the laboratory and walking next to the cable.

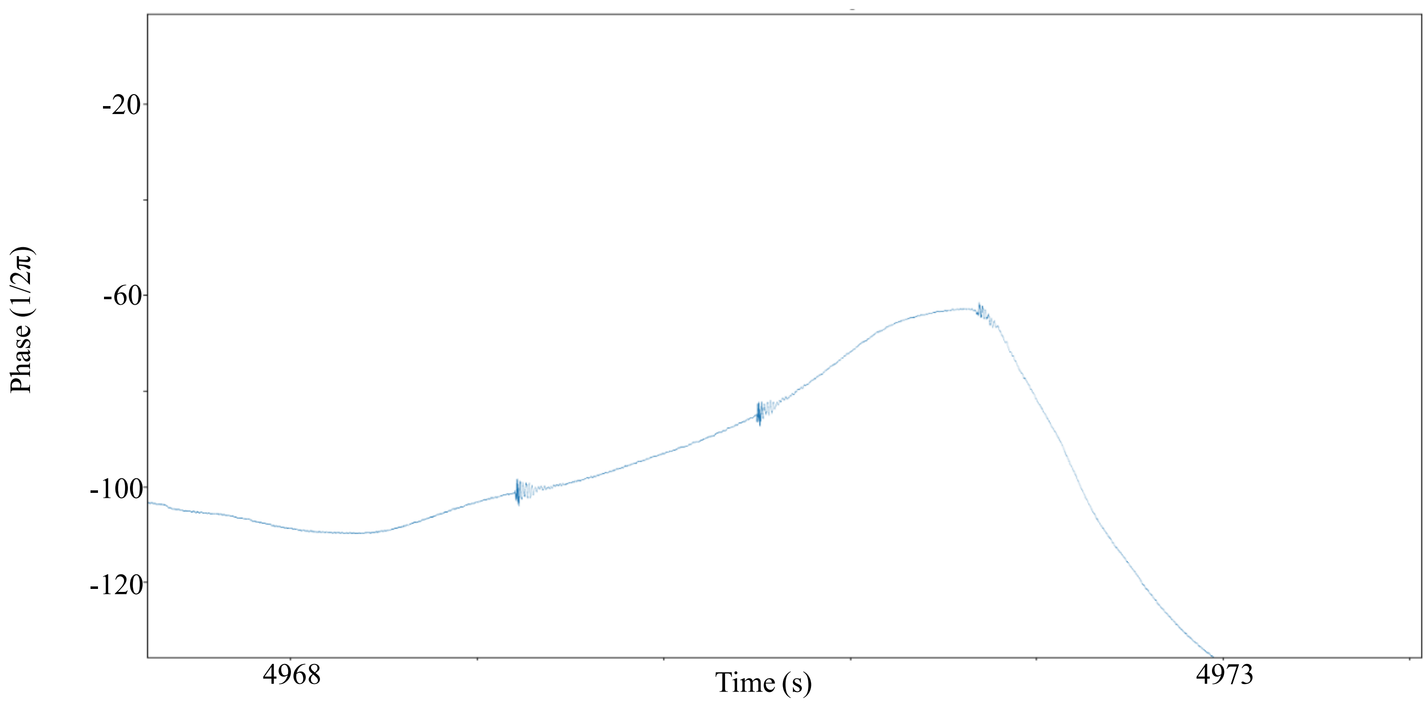

Figure 27. Three steps next to the cable (500 m fibre for sensing arm).

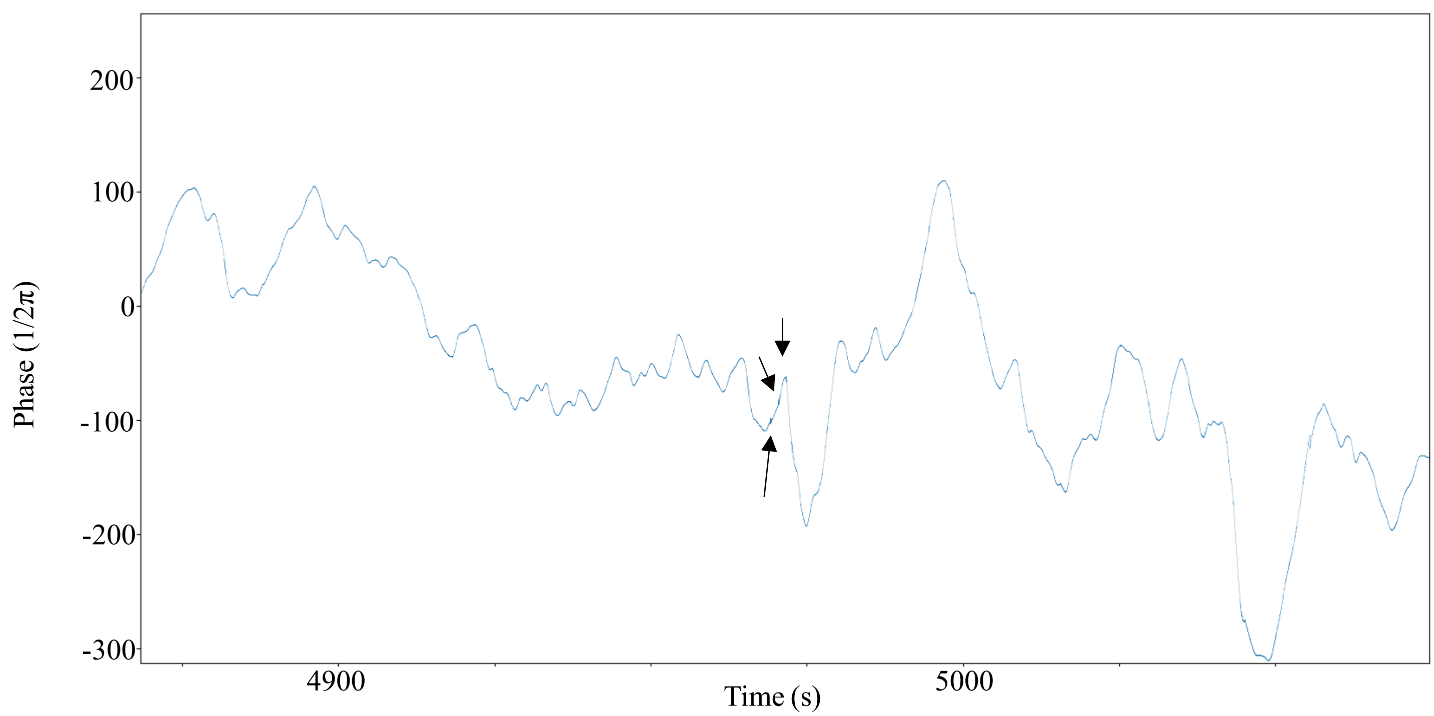

Figure 28. The steps of Figure 29 are marked with the arrows. They are difficultly distinguished from the phase oscillations overall.

Notice how the three steps are barely seen if looking at the phase on a larger view (fig.30), making it difficult for its registration, and suggesting that we will need to use spectrograms and velocity plots later. The initial vertical displacement of the steps was less than 4 in $1/2\pi$ units. This was the reason we were not able to do these measurements before the noises were cleared on section 3.3.

We will now compare the type 3 error mentioned before (fig.27.C) with these very distinctive measurements.

A person leaving the lab and closing the door is registered multiple times (still on 500m fibre setup). On fig.31 one of these events is observed. As before with the steps, the vertical displacement is not greater than 4 in the phase.

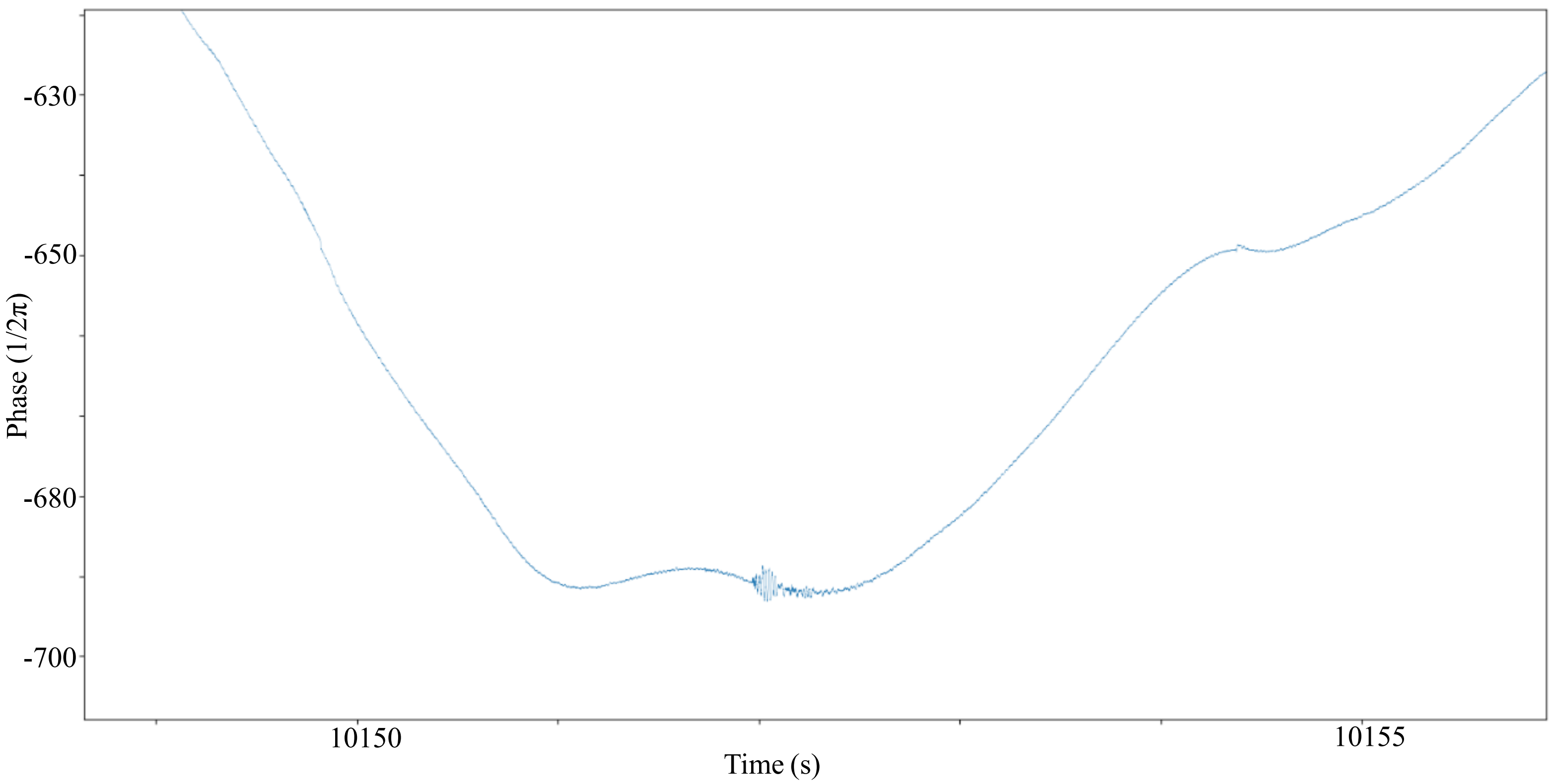

Figure 29. Phase reconstruction in which a person leaving the lab is registered.

Even if the door closing is very clear from this Figure 31, notice that the time plotted is not more than six seconds. This would complicate the detection of the event when analysing longer time periods. And so, as done with the seismometers, we will attempt to use the velocity plots and spectrograms. However, from the velocity, we will see that if the previous errors (fig.27) surround the event, they can completely hide it (fig.32). If these errors are not solved in future versions of the project, earthquake detection will be extremely difficult on these smaller fibres.

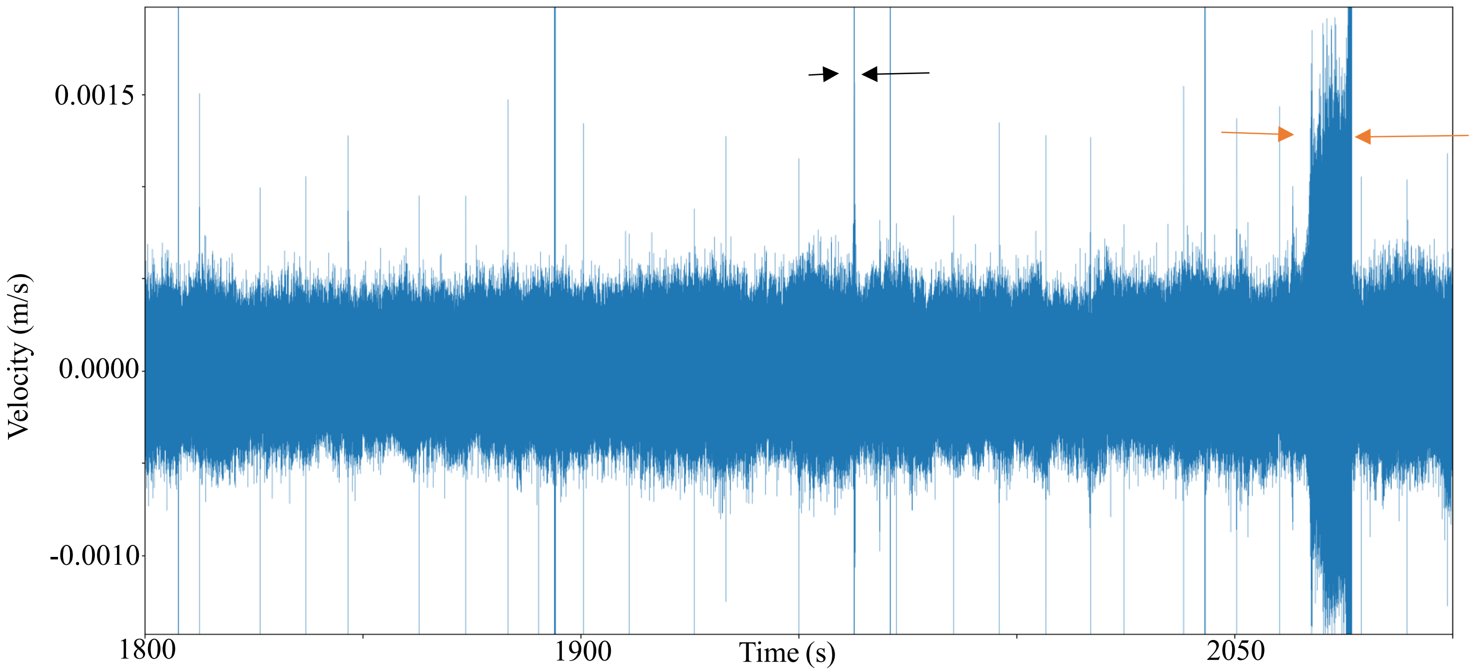

Figure 30. Velocity plot of one of the phase measurements. The exiting from the lab from is marked in black arrows, while the other peaks correspond to measurement breaks of type 1 or 2, while the orange arrows cover an error of type 3.

A distinctive measurement that can be done is the difference between night and day. This is perceived only when looking at the velocity spectrogram. The night-day transition is useful to identify some of the recurrent man-made background noises. For this, a measurement with a cable to the Main Distribution Frame (MDF) room is used. The cable goes next to air vents and finishes next to where the R9273 seismometer was installed before returning to the lab for a total distance of approximately 200m.

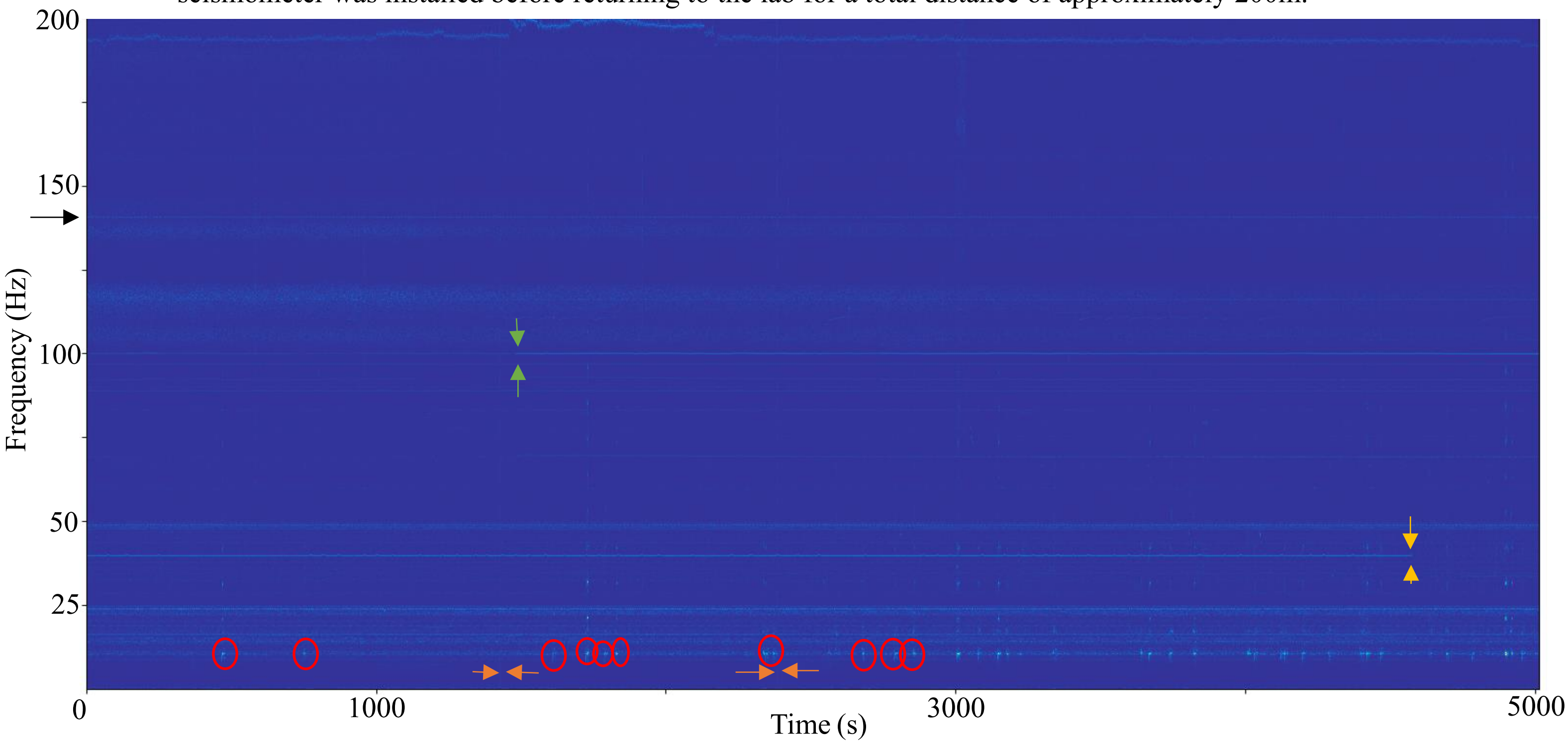

Figure 31. Velocity spectrogram measurements through the MDF room. Section 6:41am - 8:05 am. Recall lighter colours indicate higher relative intensity with respect to the other frequencies represented.

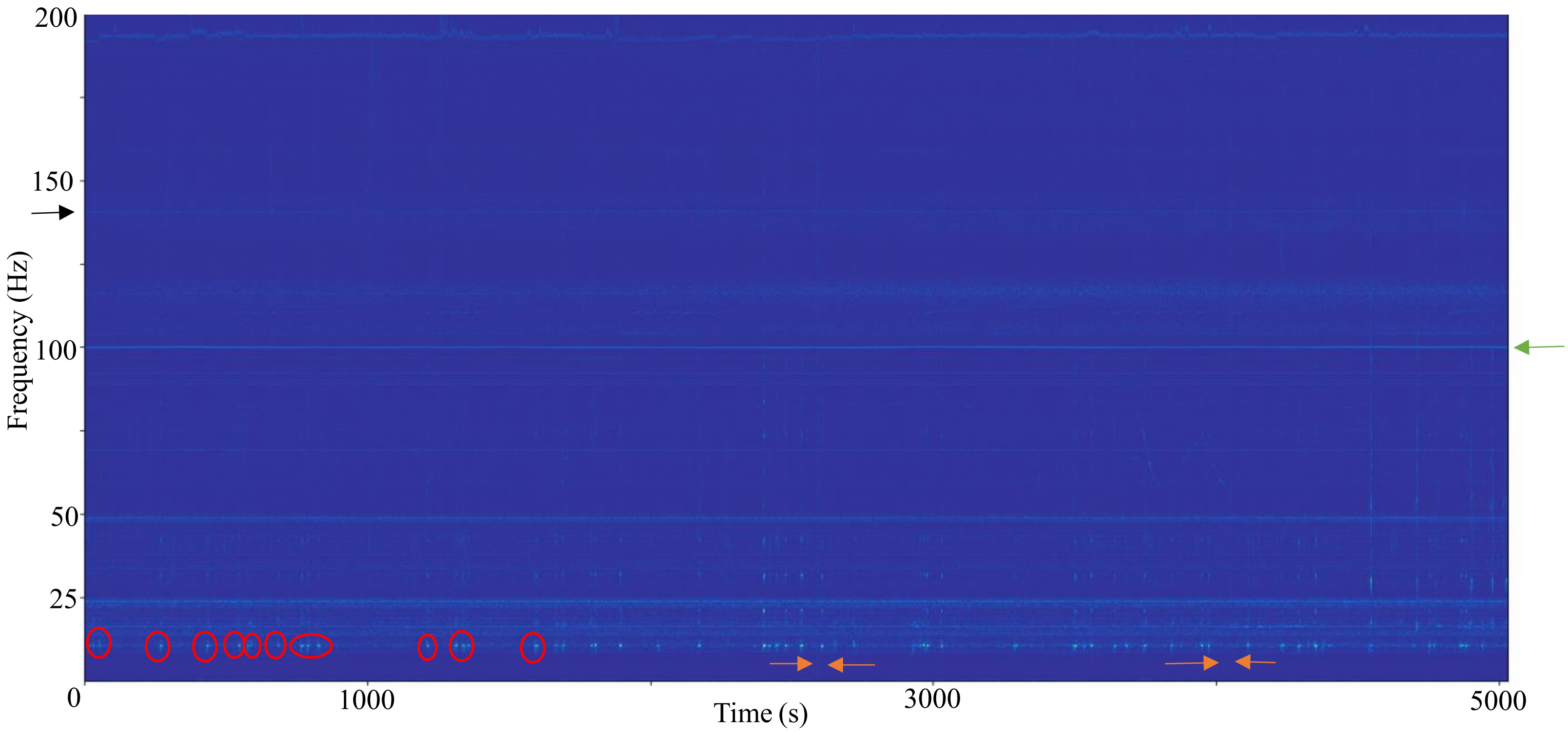

Figure 32. Continuation of fig.33 velocity spectrogram for night-day transition. 8:05 am to 9:28 am.

From these graphs the night-day transition is mostly observed by the appearance of some of the noises at around 10 Hz (red circles at the first ten groups seen on both figures, some of them contain various of these events). Those seem to become more frequent as the hours go by so the first guess is that they correspond to traffic, as noise at similar frequencies had been previously detected in all the seismographs.

Other important frequencies observed are the horizontal lines. Especially the 100 Hz (green arrows) seem to become stronger after precisely 7:05 am, while others are turned off at precise times too (yellow arrow). Some look purely mechanical such that around 140Hz (black arrows) where ten seconds on and off pattern is observed. This last one seems particular to just the MDF room. The vertical lines that reach down to almost 0 Hz correspond to type 3 errors (orange arrows), and so should be easily removed with software.

4.3. 20 km sensing arm measurements

A 20 km fibre (40km difference) was used to measure the effects of longer fibres on the phase reconstruction. The phase showed how the vertical displacement of 0.1 (fig.25) now stayed at 5. The vertical fluctuations on the measurements every couple of tens of seconds also increased to the tens of thousands (more than 100 times what was shown before on fig.25). However, the fibre is more sensible to any displacement too. We may think of it as just a change in scale. Moreover, some of the laser instability problems (fig.27) did not scale up with the change in length. The proof of it is that steps and doors are still very easily recognizable and have incremented their difference with respect to before (fig.29 versus fig.35).

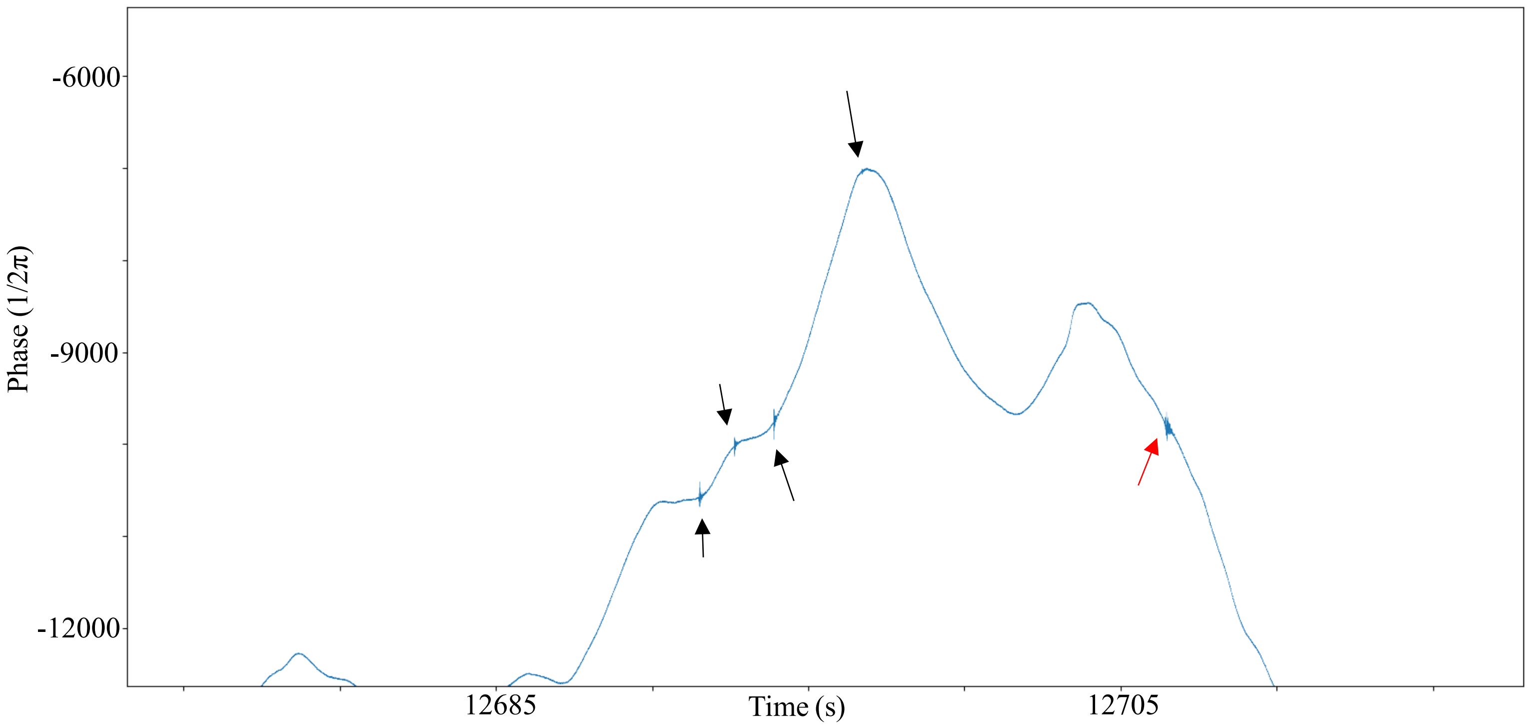

Figure 33. Measurement with the 20km fibre connection inside the lab. Steps (black) and door closing (red) are seen. Note how differently from before, the displacement of the phase is in the hundreds instead of in the tens of units.

Now, to test the full effects of the sensitivity increment, the street next to the lab was recorded, while measurements with the 20 km long fibre inside the lab were being made.

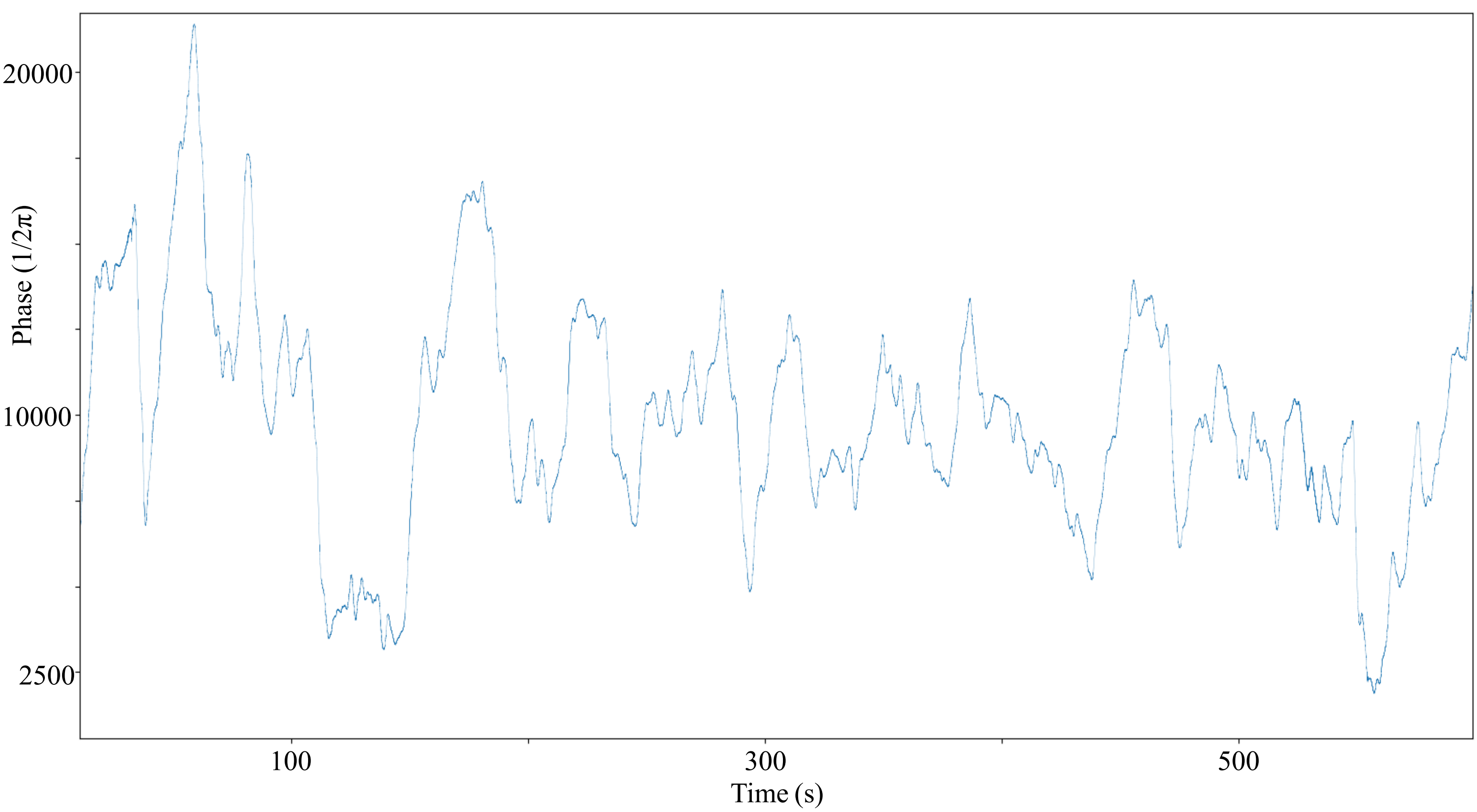

Figure 34. Measurement of the fibre while recording. Every few seconds, the phase varies by thousands of radians.

After observing the data from the phase reconstruction and from the velocity plot, nothing can be distinguished. The techniques of filtering and spectrum analysis developed on the earthquake detection code can now be applied. From those, we obtain the next spectrogram (fig.37), where we see the same dots around 10 Hz as before. By comparison with the recorded video, each of them corresponds to a bus passing approximately 10 m next to the lab building (lab is on a third floor). Smaller or slow-moving vehicles do not have any visible effect. On Figure 37, the last vertical line corresponds to a person moving a heavy cart on the same floor as the lab.

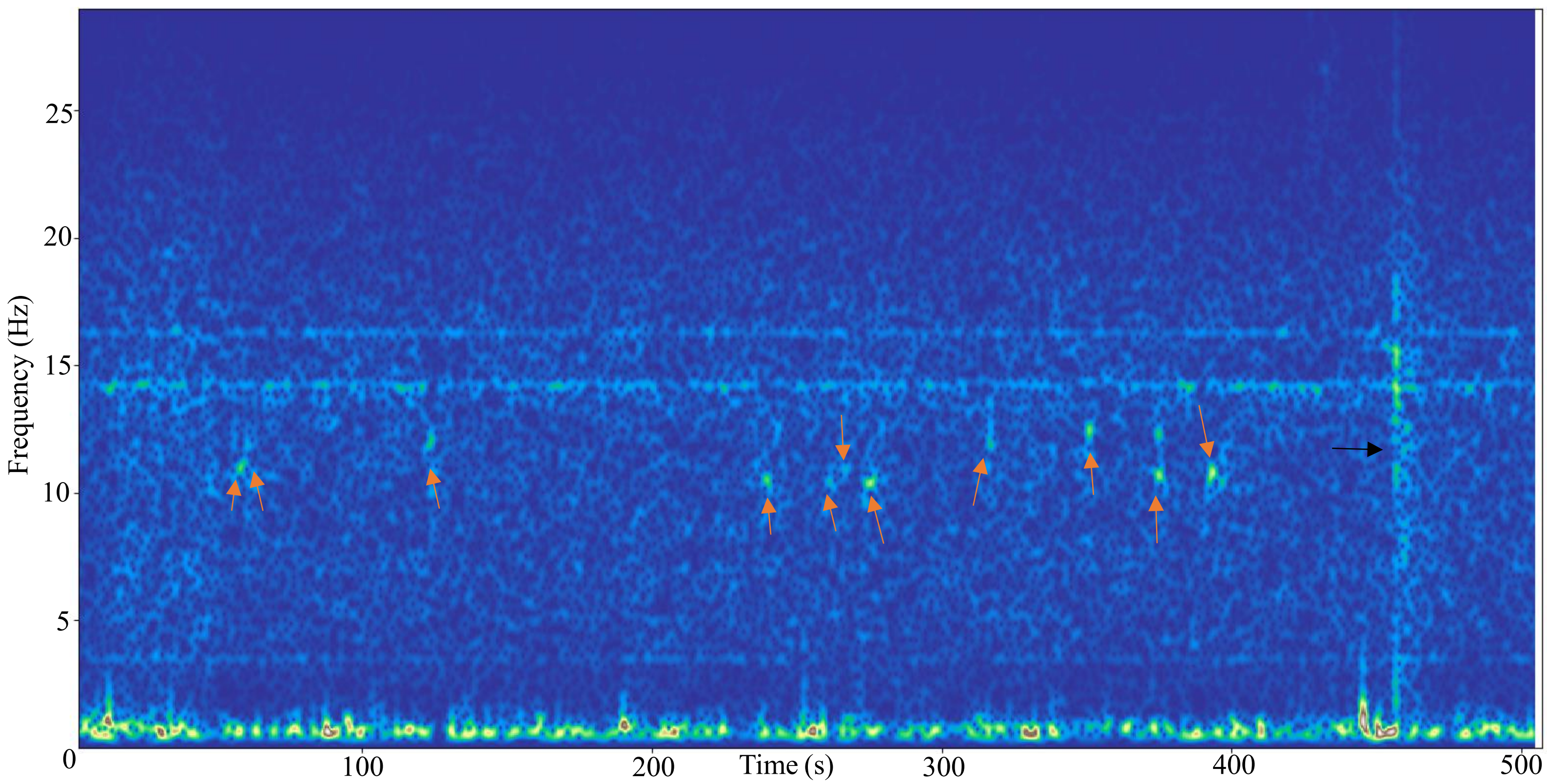

Figure 35. Extract of the measurement while recording during daytime, every bus is marked with an orange arrow, while the cart in a black one.

While the cart could be felt from inside the lab, the buses are too far away to be felt by humans. This confirms that indeed measurements of ground vibrations can be done with this set up.

During the time this configuration was tested, no major earthquakes occurred in the region. As a result, it was not possible to find any earthquakes with the long fibre. However, the possibility of being able to measure traffic (fig.37), indicates that the setup could be sensitive enough to detect strong earthquakes.

Lastly, even if the experiment can detect traffic, the type 3 errors (Section 4.1) must be resolved in the future. As seen in figure 38, they are as strong in intensity in the spectrogram as the buses. And the traffic and buses noise are expected to be more intense than most earthquakes (based on the seismographs data).

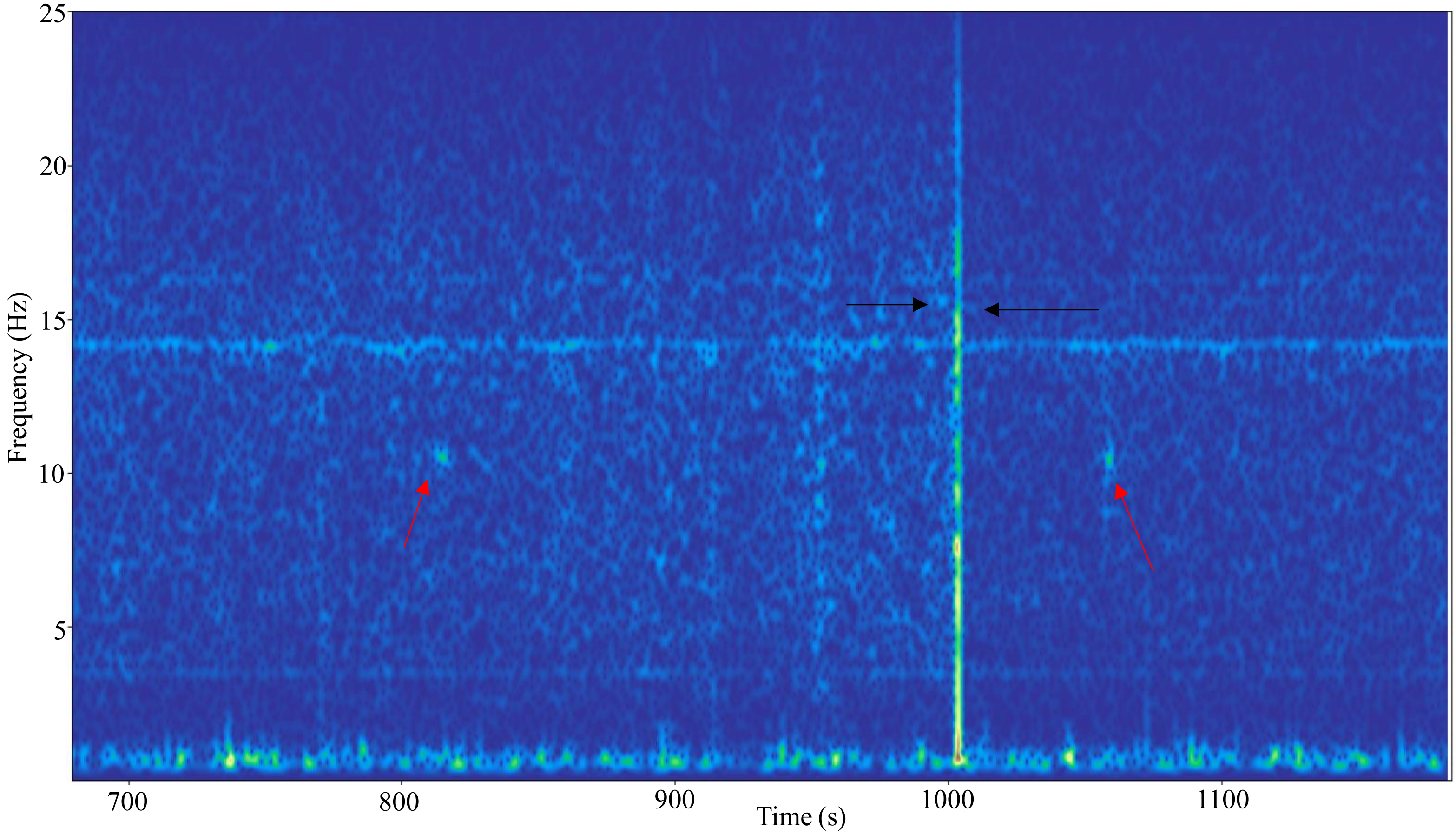

Figure 36. Spectrogram of a phase measurement on 20 km fibre. Two buses are seen (red arrows) and were confirmed by the recorded video. The type 3 error however is more visible (black arrows).

5. Summary and next steps

Initially, it was understood how the data extracted from seismographs could be used to determine the arrival of earthquake waves to the fibre sensing project. This information could later be compared with the phase reconstruction data. Moreover, the written code could help the user better interpret earthquake detection and determine the distance from a detector to the epicentre of it. Furthermore, the techniques needed to separate background noises from possible events were explored.

Then, the noises in the initial phase reconstruction data were identified, and solutions were implemented to make those measurements better. With the increased sensitivity in the fibres, detections could finally be made. More precisely, events such as the transition between night and day or traffic were registered.

As of July 2023, the setup seems to be just sensible enough to detect strong earthquakes. The most logical step would be to move it to a more silent location. Then, the laser stability problems must still be worked on, as type 1,2 and 3 errors are recurrent enough to be a concern in the measurements if small fibres are employed. Also, long deployed cables should be used to characterize noises and understand the real impact of longer lengths and city noises over the phase reconstruction.

Lastly, once a strong enough earthquake occurs, the exact pattern of seismic waves and the frequencies in which they occur in the phase reconstruction can be studied. With this, some of the triggering functions parameters and techniques described in section 2 can be easily modified. Eventually it would be possible to write an automatic detection system for the fibre sensing project.

6. Appendix

6.1. Notes on parameter selection and errors

The following notes are based on my testing of the code.

The parameters configuration that doesn't deactivate any function should be used during nighttime when trying to find near (<1000km) events and when we are sure that the data collected by the seismographs is in good conditions (does not lack information at times or includes strange noises like construction work). An example of the use of these parameters is Case 1.

The parameters configuration that deactivates the carl-sta function should be used during nighttime trying to find further (>1000km) events but of relatively large magnitude (5.5+).

The parameter configuration that only operates with the z-detect function should be used during nighttime when trying to find events that can be of the same magnitude as some of the noise spikes. Also, this is the setting that should be used to detect any events during daytime. An example of this is Case 2.

Regarding possible errors in the code, the code makes use of some of the Obspy implemented functions. The p-s picker function may sometimes raise an exception specially when in the 'just-z = True' parameter if many events need to be analysed. In case this happens, note that the user already has all the confirmed events in the variable 'eventss'. In the python console then, the user can just call 'event = eventss[position desired]' and after it copy and run from line 754 to line 794 of the code. Uncomment the plots in those lines of the code if the user wants the 18 plots for deeper analysis of that event. This is also useful when just checking a particular event of the suggested ones on the daytime analysis (the global spectrogram is always plotted to help the user though).

In addition, other external errors could stop the program if the data used from the server is missing fragments of time or was not properly uploaded to the server. If given this error, one can make sure all the data the code is running on appears properly in the raspberry data view webpage (as the MS network should not fail).

No other errors have been noted over the two months of testing.

7. Bibliography

1- Howe, B., Aucan, J., Barros, J., Bayliff, N., Fouch, M., Jamelot, A., Kong, L., Lentz, S., Luther, D. S., Marinaro, G., Matias, L., Panayotou, K., Rowe, C., Sakya, A. E., Salaree, A., Hillebrandt-Andrade, C. von, Wallace, L., & Weinstein, S. (2021). SMART Cables Observing the Oceans and Earth. OCEANS 2021: San Diego – Porto, 1–7. https://doi.org/10.23919/OCEANS44145.2021.9705851

2- Marra, G., Clivati, C., Richard, L., Tampellini, A., Kronjäger, J., Wright, L., Mura, A., Levi, F., Robinson, S., Xuereb, A., Baptie, B., & Calonico, D. (2017). *Seismology with optical links: enabling a global network for submarine earthquake monitoring*. https://doi.org/10.48550/arxiv.1801.02698

3- Nathaniel J. Lindsey, y, T Craig Dawe, and Jonathan B Ajo-Franklin (2019). Illuminating seafloor faults and ocean dynamics with dark fiber distributed acoustic sensing. *Science* **366**,1103-1107.DOI:10.1126/science.aay5881

4- Tay, W. Y. T. *2022). Fibre Sensing. [Undergraduate Thesis, NUS] NUS quantum optics publications (qolah.org)

5- Watchi, J., Cooper, S., Ding, B., Mow-Lowry, C. M., & Collette, C. (2018). Contributed Review: A review of compact interferometers. Review of Scientific Instruments, 89(12), 121501–121501. https://doi.org/10.1063/1.5052042

6- Udd, E., Spillman, W. B., & Spillman, W. B. (2011). FIBER OPTIC SENSORS: An Introduction for Engineers and Scientists. In Fiber Optic Sensors. John Wiley & Sons, Incorporated.

7- Rashleigh, S. (1983). Origins and control of polarization effects in single-mode fibers. Journal of Lightwave Technology, 1(2), 312–331. https://doi.org/10.1109/JLT.1983.1072121

8- Krischer, L., Megies, T., Barsch, R., Beyreuther, M., Lecocq, T., Caudron, C., & Wassermann, J. (2015). ObsPy: a bridge for seismology into the scientific Python ecosystem. *Computational Science & Discovery*, *8*(1), 14003–14017. https://doi.org/10.1088/1749-4699/8/1/014003

9- Chouet, B. A., & Matoza, R. S. (2013). A multi-decadal view of seismic methods for detecting precursors of magma movement and eruption. Journal of Volcanology and Geothermal Research, 252, 108–175. https://doi.org/10.1016/j.jvolgeores.2012.11.013

10- Withers, M., Aster, R., Young, C., Beiriger, J., Harris, M., Moore, S., & Trujillo, J. (1998). A comparison of select trigger algorithms for automated global seismic phase and event detection. Bulletin of the Seismological Society of America, 88(1), 95–106. https://doi.org/10.1785/BSSA0880010095

11- Akazawa, T. (2004). A technique for automatic detection of onset time of P-and S-Phases in strong motion records,13th World Conference on Earthquake Engineering. http://www.iitk.ac.in/nicee/wcee/article/13_786.pdf

12- Kennett, B. L. N., & Engdahl, E. R. (1991). Traveltimes for global earthquake location and phase identification. Geophysical Journal International, 105(2), 429–465. https://doi.org/10.1111/j.1365-246X.1991.tb06724.x

13- Kanamori, H. (1977). The energy release in great earthquakes. Journal of Geophysical Research, 82(20), 2981–2987. https://doi.org/10.1029/JB082i020p02981